ULTRASOUND-BASED ESTIMATION OF SOFT TISSUE MECHANICAL PROPERTIES IN SUB-HERTZ FREQUENCY RANGE

A THESIS
SUBMITTED TO THE FACULTY OF
UNIVERSITY OF MINNESOTA

BY

ALIREZA NABAVIZADEHRAFSANJANI

IN PARTIAL FULFILLMENT OF THE REQUIREMENTS
FOR THE DEGREE OF
DOCTOR OF PHILOSOPHY IN BIOMEDICAL INFORMATICS AND COMPUTATIONAL BIOLIGY

Prof. MOSTAFA FATEMI

AUGUST 2016

Acknowledgements

I would like to express my deep gratitude and appreciation to my advisor Dr. Mostafa Fatemi and co-advisors Dr. Matthew W. Urban and Dr. Claudia Neuhauser for their encouragement, patience, support and guidance through this thesis research. I would like to thank my other thesis committee members as well, Dr. Mohammad Mokbel and Dr. Azra Alizad.

I would like to thank Dr. James Greenleaf and the rest of the Mayo Clinic ultrasound laboratory members for their instrumental role in successful completion of this thesis work. I am obliged to Randall Kinnick for his experimental support and expertise, Thomas Kinter for computer software support and Jennifer Milliken for administrative aid. I also would like to acknowledge Dr. Carolina Amador Carrascal for her scientific contribution, Bo Qiang and Dr. Viksit Kumar for their simulation support, Duane Meixner for his sonography guidance and Adriana Gregory for her assistance in patient study. Above all, I would like to thank Dr. Mahdi Bayat for his support, perseverance and scientific guidance during my thesis work.

I am also thankful to all the staff of the University of Minnesota in Rochester, especially Gail Sauter and Erin Spencer for their secretarial assistance.

I would like to thank the Larsen, Kvernen, Richardson and Galanits families. Whenever I think about them, I am reminded of this sentence: “A true friend won’t let you face tough times alone.”

I would like to thank my parents and my only sister from the bottom of my heart for their support and encouragement throughout my education, for providing me with the opportunity to follow my dreams and for the love to make them reality.

Dedication

I dedicate this thesis to my parents.

Abstract

Differentiating between benign and malignant breast tumors is the main purpose of this dissertation. Currently, biopsy is the most practical and reliable way. However, two disadvantages are associated with this method. First, as biopsy is an invasive method, pain and discomfort that patients experience are unavoidable. Second, biopsy is based on small samples that are taken locally; thus it is not able to produce a reliable map of a large area of tissue.

Nearly 70% of suspicious cases that are referred for breast biopsy turn out to be benign, not malignant, which means it was unnecessary for those patients to undergo this invasive procedure with all the aforementioned side effects.

Technological advances in imaging are prime candidates to replace biopsy with a noninvasive, affordable, more accessible procedure with no side effects. Ultrasound shares all these characteristics. In addition to these benefits, ultrasound-based methods can assess the local mechanical properties of tissue, making this modality a promising tool for differentiating between malignant and benign cases in breast patients. My Ph.D. dissertation focused on developing a device combined with ultrasound to discriminate between benign and malignant breast tumors according to their mechanical properties. Our patient study in the Mayo Clinic has confirmed the effectiveness of this device in discriminating between benign and malignant cases.

Both the hardware and software of this device were designed and developed at the Mayo Clinic ultrasound lab. In this dissertation the whole process of designing and using this device will be explained through five Chapters.

Table of Contents

List of Tables

List of Figures

Chapter 1:

Introduction to ultrasound-based viscoelasticity method

1.1 Background

Palpation or compressing the tissue by hand to evaluate its stiffness or detect abnormalities such as stiff nodules inside the tissue is a very common method that physicians use to evaluate the healthy state of the tissue. Palpation first was introduced by Hippocrates and he showed that there is a strong relation between stiffness and tissue health [1]. Often in organs like breast the change in stiffness is an indication of cancer and estimation of the stiffness is a vital step in diagnosis and treatment [2-8].

Palpation is still the easiest and most common method in evaluating the tissue stiffness, but it can be applied only for large and superficial stiff masses. It is not sensitive enough to detect the masses in primary stage or those located in deeper parts of tissue. Other factors like repeatability and accuracy should be considered when it comes to subjective tumor evaluation technique such as palpation.

A standard and common method for detection of various cancerous diseases is biopsy which inspects the cancerous cells and their histology. But it is an invasive technique which can cause pain and discomfort for the patient and also can be costly and time consuming. Another negative aspect of biopsy is its restricted area of examination [9, 10].

In most cases after doing the biopsy it was found that it was not necessary. In order to minimize the number of unnecessary biopsies, developing a lower cost, noninvasive method is essential [2].

Nearly twenty years ago Professor Jonathan Ophir came up with new noninvasive imaging method called “Elastography” or elasticity imaging

[11]. This method made it possible to obtain an estimation of elastic modulus and strain based on measuring displacement gradient, or strain, by applying ultrasound imaging and external compression together. Local strain estimation based on ultrasound images appeared to be a solid criterion to differentiate the stiff from soft part in a medium because of the phase sensitive nature of ultrasonic data it is possible to detect a very small motion on the order of microns [11].

Due to the ease of use and effectiveness of elastography, this method has gained a lot of attention; it is the basis of some other pioneering techniques [12] that are still growing. The aim of elastography is to describe the mechanical properties of medium. However, the primary assumption behind the elastography method is that the medium is purely elastic [11]. Considering the viscoelastic properties of medium based on monitoring the medium behavior through time can add more information about the mechanical properties of tissue. [12].

One of the techniques that originated from elastography but considers the viscoelastic behavior of the medium is the creep test which can be performed using indentation and compression [12]. There are some commercial instruments like the BOSE Electroforce (Bose , Eden Prairie, MN) which can measure the creep response of the material or tissue samples very accurately; however, their mechanism of measuring creep response is based on the surface displacement measurement which means this device is not able to differentiate between two different regions in one medium. It is also not possible to use such devices in a clinical setup.

Professor Michael Insana can be considered as a pioneer for noninvasive *in vivo* application of the creep test in breast patients [13, 14]. Prior to that work, a comprehensive study was performed on tissue mimicking phantoms

for validating and establishing this technique. Finally in his last work on a small group of nonpalpable breast patients he proved that the creep test has the ability to differentiate between the malignant and benign, especially fibroadenoma cases, but in all of his patient studies the force was applied manually [14].

In the next section I will explain briefly about the elastography method and creep test.

1.2 Elastography

In elastography, the parameter that describes the tissue stiffness is Young's modulus (E) which can be described by:

$$E = \frac{\sigma}{\varepsilon} \qquad (1.1)$$

where σ is stress and ε is strain. This equation shows that the Young's modulus of tissue can be assessed by applying stress and measuring the strain or the deformation resulting from stress.

In static elastography, the method that Prof. Ophir proposed [11], equation (1.1) is its essential part. In this way ultrasound is employed to estimate the strain resulting from the external stress which can be applied by pressing the ultrasound probe on top of the tissue [11]. This process is helpful in evaluating the tissue because it can discriminate the soft part from the stiffer part due to differences in deformation that can occur; for the soft part this deformation is much higher than the stiffer part [11]. This contrast between stiff and soft parts in tissue has a diagnostic value [15].

The local strain, ε, in equation (1.1) can be measured by ultrasound techniques, but the local stress, σ, is always a challenging part. It is possible

to measure the total force or stress on the top of the tissue but locally within the object it is difficult or impossible. When it comes to a heterogeneous medium like tissues it is more complicated. Thus in the static elastography methods it is not possible to measure the Young's modulus quantitatively. This method is based on the strain maps in which the stiffness contrast between different parts can be depicted rather than the Young's modulus of each region [11].

One of the main applications of strain imaging is in creep test study which explores the viscoelastic properties, retardation times, of the medium.

1.3 Viscoelastic Vs. elastic response

The aim of the elastogrpahy, as explained before, was to evaluate the tissue local stiffness noninvasively. It is hypothesized that malignant tumors grow much stiffer than benign cases. However, from tissue biomechanics, the mechanisms leading to a breast lesion not only manifest as higher elasticity but also a significant change in viscosity compared to normal tissue [16].

From the molecular biology point of view, it has been proven that in the process of malignant tumor development the epithelial cell sends and receives molecular signals to and from surrounding stromal cells [17] this process can induce structural modifications to the extra cellular matrix (ECM) which will change the extracellular fluid's viscosity and alter the viscoelastic properties of tissue. Changes in cellular mechanical environment are a sign of disease progression [18], [19].

Thus monitoring the time-dependent viscoelastic response, or creep test, of breast tissue can provide more diagnostic information compared to the static elastography method.

1.4 Ultrasonic Creep test

The ultrasonic creep test can be divided into two categories based on the excitation method: internal and external creep. As is obvious from the name, in both of them the deformation is detected by ultrasonic methods. In internal ultrasonic creep, the excitation is acoustic radiation force [20] and similar to other methods like Monitored Steady-State Excitation and Recovery (MSSER), [21], and its following version (VisR) imaging methods,[22], which are slightly different from the internal creep test . All of these methods generally deal with the viscoelastic response of the medium.

In the external ultrasonic creep test, excitation is applied externally via a compression surface which is usually the ultrasound probe equipped with a surface extender [14], and it is the main focus of this dissertation.

1.5 Ultrasonic external Creep test

The viscoelastic creep response of tissue can be detected by ultrasonic methods. While the ultrasound probe is pressed on the surface of the imaging phantom or tissue the movements of the internal structures will be tracked using the radiofrequency data from conventional pulse-echo ultrasound and speckle tracking algorithms. A step force with amplitude of 1.5-6 N is applied for 10 to 20 seconds while the movement of the tissue will be recorded through the acquired echo data from which a series of strain images can be calculated. It should be noted that while the constant force is applied the tissue will gradually deform. This slow deformation of tissue under load is called “viscoelastic creep”, which is defined by the viscoelastic properties of the phantom or tissue. These tissue properties can be explored by analyzing the time series of strain images. Because the frequency stimulus of the mechanical force for creep response of the soft tissue or

hydro polymer is different for the dynamic and quasi-static methods [11], therefore, these different methods will provide independent information [14]. Figure 1.1 shows the steps in the procedure to obtain the creep response.

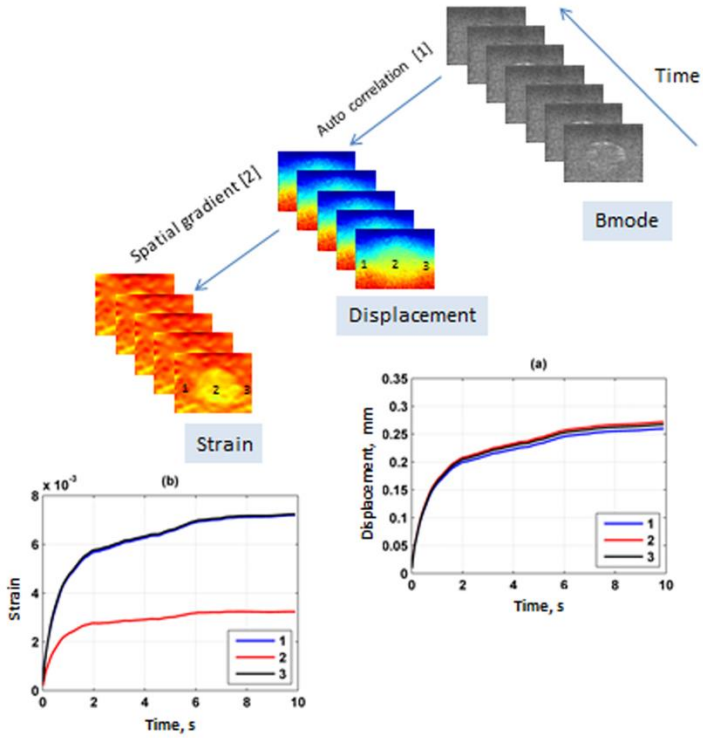

Figure 1.1 Creep process including multi-compression radiofrequency echo acquisition, strain image formation, and displacement and strain behavior of three specified points inside the inclusion, 2, and background part, 1, 3.

The strain curve is plotted over the time series of strain images to generate the viscous creep curve. Each creep curve is computed from each pixel or a small group of pixels, and from this resulting creep curve it is possible to extract viscoelastic, VE, parameters by fitting a rheological model to the phantom data [23]. Typically, the data acquisition takes 15-20 seconds. For this data length a first-order discrete Kelvin-Voigt rheological model [13,

14, 23] is used as a model for characterizing the material behavior, which is one of the methods for analyzing the creep behavior in the time domain.

$$\varepsilon(t) = \varepsilon_0 + \varepsilon_1\left(1 - e^{-\frac{t}{T_1}}\right) \qquad (1.2)$$

In Eq. (1, 2), ε_0 is the instantaneous elastic strain, which occurs immediately after compression [14]. The parameter ε_1 is the amplitude of the exponential creep curve. The constant T_1 characterizes the delay in the full strain response called the retardation time and in this model can be described as the ratio of the viscosity over elasticity. Based on a previous study, the T_1 factor has the ability to discriminate between malignant and benign tumors as the results show the T_1 time for malignant is much shorter than for benign tumors [14].

1.6 Displacement and strain profile measurement

Applying a cross-correlation method and optical-flow algorithm to measure the particle velocity are common method in elastography [24, 25, 26, 27, 28].

In our methods we will use autocorrelation methods due to high speed capability of Verasonic machine (Verasonics, Kirkland, WA) in producing the in-phase/quarter (IQ) data which is used to track the fast tissue deformation [30].

As was explained in the previous section, measuring the local displacement based on the ultrasound IQ data is an essential part in calculating the strain which is the base of a creep response. Loupas *et al.* [30] described the one-dimensional/two-dimensional or 1D / 2D autocorrelation method, equation (1, 3), for particle velocity measurement.

$$V \cong \frac{c}{2} \frac{\frac{1}{2\pi T_s} tan^{-1}\left\{\frac{\sum_{m=0}^{M-1}\sum_{n=0}^{N-2}[Q(m,n)I(m,n+1) - I(m,n)Q(m,n+1))]}{\sum_{m=0}^{M-1}\sum_{n=0}^{N-2}[I(m,n)I(m,n+1) + Q(m,n)Q(m,n+1)]}\right\}}{2\frac{1}{2\pi t_s}\left(2\pi f_{dem} + tan^{-1}\left\{\frac{\sum_{m=0}^{M-2}\sum_{n=0}^{N-1}[Q(m,n)I(m+1,n) - I(m,n)Q(m+1,n)]}{\sum_{m=0}^{M-2}\sum_{n=0}^{N-1}[I(m,n)I(m+1,n) + Q(m,n)Q(m+1,n)]}\right\}\right)}$$

(1.3)

In this equation the IQ data is used and T_s and t_s are the fast and slow axis sampling periods, respectively. Thus the displacements can be estimated by integrating the particle velocity in time.

1.6.1. Displacement Validation

In order to validate the displacement tracking method a simple translational test was done on a uniform phantom in a water tank. A L7-4 linear array transducer (Philips Health care, Andover, MA) was moved vertically toward a uniform phantom in a water tank with the speed of 1 mm/s for 10 seconds while a Verasonics machine was used to record a sequence of RF data using plane wave imaging. The ultrasound transducer did not touch the phantom at the end of its movement. Because there were no scatterers in the water tank a blue layer appeared on top of the displacement map indicating zero displacement however the phantom part getting closer to the transducer with same speed as is clear in Figure 1.2.

The one-dimensional/two-dimensional or 1D/2D autocorrelation methods, equation (1.3), were used for measuring the particle velocity and displacement. Figure 1.2 shows the displacement map which results from translational motion.

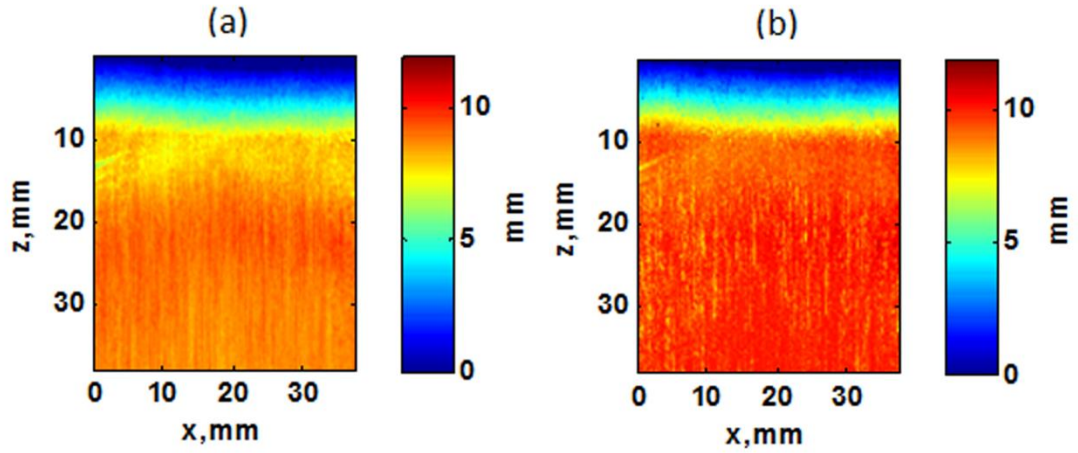

Figure 1.2 Displacement profiles. (a) Displacement map after applying 1D autocorrelation method. (b) Displacement map after applying 2D autocorrelation method

It is obvious in Figure 1.2 that the 2D autocorrelation, figure 1.2(b), operates more accurately than 1D autocorrelation. The displacement measurement by ultrasound and 2D autocorrelation method is equal to the total displacement of the probe. This experiment is a solid validation of performance of 2D autocorrelation method for displacement measurement.

1.7 Problems and Specific Aims

The main goal of the dissertation is designing a fully automatic device to assist with differentiating between the malignant and benign tumors in breast tissue based on their creep response and retardation time which mostly deals with viscoelastic properties of this medium.

Based on the results of a creep study on a small group of nonpalpable tumors in patients, this method has the ability to differentiate between the malignant and benign tumors in breast patients [14].The main problem is that the creep test in this study is done manually by a sonographer. Although this method proved to be accurate [23,31], it may raise the question of sonographer training, hand jitter, and reproducibility. Another problem with this study is

its analysis of the creep response. Model-based methods are very common for assessing the viscoelastic properties of the medium [14, 22]. However, using these methods has its own disadvantages: 1) The models sometimes are not the best representation of the data and it may force the user to approximate their data into a prescribed form or applying bias on data. 2) To fit the data to the model well sometimes it requires a very large number of fitting parameters which may take a long time. Also generally modelling a complex medium like tissue with a simple model like Voigt or Maxwell including just springs and dashpots can always be questionable [32].

In this PhD dissertation we will explain the design and validation of a new device which has the ability to apply an approximate step force to excite a creep response in gelatin phantoms and in breast patients. This device will help to decrease the aforementioned errors like hand jittering, reproducibility and have a better control on force and its speed comparing to hand-held method.

Also a model-free method that will be explained later to evaluate the creep response of these medium can help to work directly with real data instead of their fitting curve and its disadvantages that were mentioned before.

Chapter 2:

Automated Compression Device for Tissue Viscoelasticity Imaging

This is a paper submitted for publication with these co-authors:

Alireza Nabavizadeh[1,2], Randall R. Kinnick[2], Mahdi Bayat[2],Carolina Amador[2], Matthew W. Urban[2],Azra Alizad[2], Mostafa Fatemi[2]

Introduction

Viscoelastic mechanical properties have been linked to pathology of soft tissue [8, 33, 34]. An explanation for this is the alteration of the extracellular matrix in diseased tissues, which can manifest as changes in tissue mechanical properties [23, 35].

Mechanical properties of the medium can be assessed by creep test. Creep test is a standard method to evaluate the continuous deformation of a material under a constant stress [36]. The creep response of a material is the result of applying a step-force excitation. This force causes a transient strain response that is governed by the viscoelastic properties of the material [13, 37]. Rheological models are usually used to relate the stress-strain curves to the mechanical properties of the sample under test. Employing creep test in different imaging modalities like ultrasound [17, 23, 38], MRI [39, 40] to evaluate the viscoelastic properties of the medium has been proposed by a number of investigators. For this purpose, compression devices have been designed for such imaging modalities [23, 39]. Other investigators [41-46] have proposed various compression devices for elasticity imaging, where such devices are mainly designed for testing tissue at its rest position after the compression. Tissue compression has been also investigated in the context of poroelasticity [47, 48]. However, these studies aimed at measuring stress relaxation response of the medium.

Hand-held compression method has been discussed in [13, 14] for *in vivo* creep test employing ultrasound imaging. However, manual compression is usually accompanied with noise due to hand jitter, which may reduce the reproducibility and repeatability of this method.

We are interested in the viscous response of the tissue, for which we need to study the temporal response of tissue under a constant stress. The goal of this study is to design and validate a fully automatic device with the ability to apply an approximate step force to excite the viscoelastic creep response in tissue while allowing *in-vivo* ultrasound image acquisition during the transient response of tissue. To validate the device we will compare its performance with a standard mechanical testing device and measure the related error. The long-term goal of this study is to employ this device to conduct creep test on a group of breast patients.

The remainder of this Chapter is organized as follows. In section one, we provide an overview of the rheological techniques for modeling tissue deformations under creep-like tests and highlight the hardware requirements for performing such tests. In section two, we explain the details of the compression device that is specifically designed to apply step-like stress on tissue. In the next section, the function of this device is validated by comparing its results with those of a standard mechanical testing instrument using tissue-mimicking samples. Section 4 is devoted to integration of the compression device with a programmable ultrasound machine for viscoelasticity imaging based on ultrasound strain estimation. We discuss the results of the validation tests as well as viscoelasticity imaging in the next section. The paper concludes with a brief summary of the results and future applications of the device.

2.1 Methods

2.1.1 Creep Response of Material

Under an external stress, material deformation can be modeled using the constitutive equations from continuum mechanics. Simplified models such as generalized Kelvin-Voigt model are shown to be suitable in the case of uni-axial constant stress on hydrogels and their creep responses are shown to be close to those of soft tissue [23].

For each point inside the material the strain-stress relationship is

$$\varepsilon(t) = \int_{t_0}^{t} D(t-\tau)d\sigma(t) \qquad (2.1)$$

where $\sigma(t)$ is the applied stress, $D(t)$ the creep compliance and $\varepsilon(t)$ is the resulting strain. For the generalized Kelvin model, the creep compliance may be expanded as

$$D(t) = \frac{1}{E_0} + \sum_{r=1}^{n} \frac{1}{E_r}(1 - e^{\frac{-t}{T_r}}) \qquad (2.2)$$

where η_r and E_r are the viscosity and elasticity coefficients and $T_r = \eta_r/E_r$ is the r^{th} retardation time [48]. In the creep test the stress applied at $t = t_0$ can be modeled as

$$\sigma(t) = \sigma_0 u(t - t_0) \qquad (2.3)$$

where $u(t)$ is the Heaviside function and σ_0 is the constant stress.

Using (2.2) in (2.1) with applying the input stress as defined in (2.3) the general creep response can be written as

$$\varepsilon(t) = \varepsilon_0 + \sum_{r=1}^{n} \varepsilon_r \left(1 - e^{-\frac{(t-t_0)}{T_r}}\right) \qquad (2.4)$$

where $\varepsilon_0 = \sigma_0 u(t - t_0)/E_0$ is the elastic response and $\varepsilon_r = \sigma_0/E_r$ is the amplitude of the contribution of the r^{th} viscoelastic term.

The number of exponential terms, *n*, depends on the complexity of the material and the observation time scale. For example, a second order Kelvin-Voigt model [23] was used to analyze only the creep response of tissue. In the present study, we will use a second-order Kelvin-Voigt rheological model to model the creep response as

$$\varepsilon(t) = \varepsilon_1\left(1 - e^{\frac{-t}{T_1}}\right) + \varepsilon_2\left(1 - e^{-\frac{-t}{T_2}}\right) \qquad (2.5)$$

Equation (2.5) models the response in terms of two retardation times T_1 and T_2 and the corresponding amplitudes ε_1 and ε_2 , respectively.

In practice, it is not possible to apply a step force and study its response. It is, however, possible to approximate the step force with a ramp-and-hold force, where the speed of the ramp is adjusted to suite the response of the material under test. The ramp speed should be chosen fast enough such that the initial elastic response of material can be easily separated from the slow creep response and can be considered as a step instead of ramp [50].

2.2 System Design

In almost all commercial mechanical testing machines, the theoretical step stress required for the creep test is replaced by a highly controlled ramp function. However, the speed of such ramp stress should be high enough to be able to capture the shortest retardation times of the material under the test.

The aim of this work is to design a compression device that is able to create such ramp forces with the additional feature of housing an ultrasound probe for continuous strain imaging during the test.

A schematic of the device is shown in Figure 2.1. This device is equipped with an ultrasound probe which can record the local deformation of tissue under stress.

This device consists of a lightweight, miniature linear actuator, (MR20LS with 2 mm lead screw, PBC Linear, Roscoe, IL), driven by a brushless DC (BLDC) servomotor, (RP17M brushless DC servomotor with encoder, Electrocraft, Dover, NH) which moves a commercial ultrasound probe together with a pressure plate rapidly onto the material or tissue until a preset force level on the probe face is reached. The actuator control system uses 4 small load sensors (FSS015, 15 Newton range, Honeywell, Bloomington, MN), embedded in a back plate, to measure the applied force. The control system maintains the preset force level constant for a predetermined period of time, typically about 10-100 seconds. When the creep measurement is complete, the actuator automatically retracts the probe.

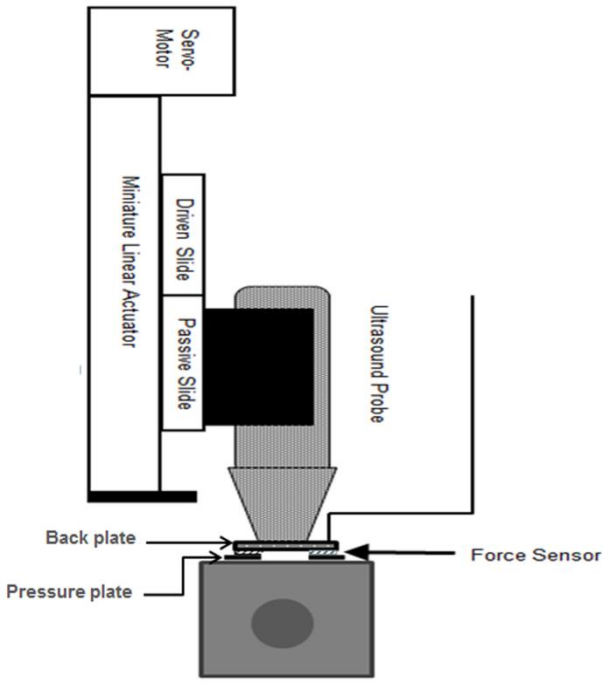

Figure 2.1. Automated compression device. The device consists of an actuator, driven by servomotor, which moves an ultrasound probe rapidly into the material or tissue to be measured until a preset force level on the probe face is reached. The actuator control system uses small force sensors embedded in the back plate, attached to and surrounding the probe face to adjust the probe position as necessary to maintain the preset force level constant for a predetermined period of time. When the creep measurement is complete, the actuator automatically retracts the probe.

The back plate is custom fit to the probe using a liquid castable plastic material (SmoothCast 300, Smooth-on, Inc., Easton, PA). The four small load sensors are sandwiched between the back plate and the pressure plate. Figure 2.2 shows the position of the load sensors at the 4 corners of the pressure plate. Thus, as the motor is applying the compression on an object, the resulting resisting force from the object is transferred to the load sensors by the pressure plate. There is a rectangular hole at the center of both plates that allows the probe face to come though such that the probe face stays at the same level as the pressure plate. This hole is covered with a thin acoustically transparent membrane that lets the ultrasound beams propagate through.

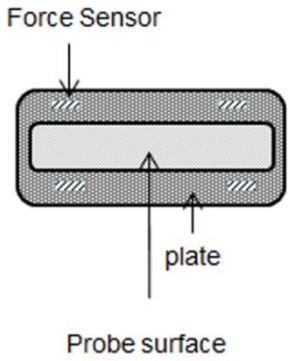

Figure 2.2 This figure shows the probe surface and the pressure plates as well as 4 force sensors positioned at the 4 corners of the pressure plate. This figure shows the front view including both pressure plate with membrane. The load cells are located between the pressuer plate and the back plate (not shown).

The four load sensors are symetrically located at the four corners of the plates . The total force is calculated by averaging the outputs of the sensors. The solid pressure plate transfers any pressure from the medium to the load sensors. Non-uniform contact between the pressure plate and the medium may result in unequal loading on the sensors. However, because the outputs of the sensors are averaged, the total output will still correspond to the total force applied to the medium. The overall dimensions of the device is 31 cm x 7 cm x 5.5 cm (length x width x depth).

2.3 Results:

2.3.1 Validation of the Automated Compression Device

2.3.1.1 Force measurement

In order to validate the compression device, we used a standard mechanical testing instrument (Bose ElectroForce®, Eden Prairie, MN) to apply force and record the resulting displacement and repeated the same procedure with automated compression device, then compared the results. We used a forcing function in the form of ramp-and-hold with 3 N final force and 18 N/s ramp rate (ramp duration of 1/6 seconds). We experimentally

determined that 18 N/s ramp is the maximum ramp speed that can be used without any ringing effects for the gelatin phantoms used in our experiments. Figure 3 shows the Bose instrument schematic.

Creep tests were performed on a homogenous tissue-mimicking phantom. To construct the phantom 13.7 grams of gelatin (Sigma-Aldrich, St.Louis, MO), 60 mL Vanicream Lite (Pharmaceutical Specialties, Inc., Rochester, MN), 0.3 grams of agar (A5306, Sigma-Aldrich), 3 grams of cellulose (Sigma-Aldrich) for ultrasound scattering and 3 grams of potassium sorbate (Sigma-Aldrich) as a preservative, were dissolved in enough water to make the total solution volume equal 300 mL. Phantom dimensions were 4x6x2 cm (length x width x height).

We tested the same phantom with our compression device and with the Bose system with similar force and ramp functions. The surface displacement data resulting from Bose system and the compression device outputs were recorded for 85 seconds.

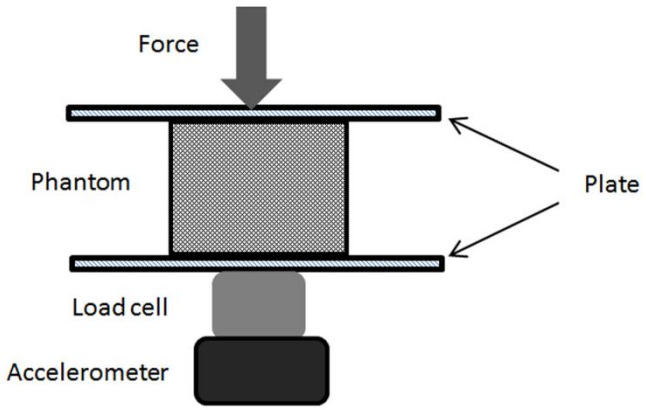

Figure 2.3 Bose instrument block diagram including two plates with the force applied on top. There is a load cell at the bottom to measure the applied force and an accelerometer at the bottom of the load cell to compensate for the inertia.

It should be noted that phantom dimensions are smaller than the pressure plate in the compression device and also smaller than the plate of the Bose

instrument; therefore, the compression is applied similarly on the entire top surface of the phantom in both cases. This allows for minimal boundary condition effects and thus the results would be comparable for both machines. There were no slippery boundaries involved.

Figure 2.4 illustrates the load (force sensor output) from our compression device and the Bose instrument at force level of 3 N with 18 N/s ramp speed. Figure 2.4(a) shows the entire force signal. In Fig. 2.4(b), just the initial 10 seconds is depicted. Both devices reach their final force values in a fraction of second.

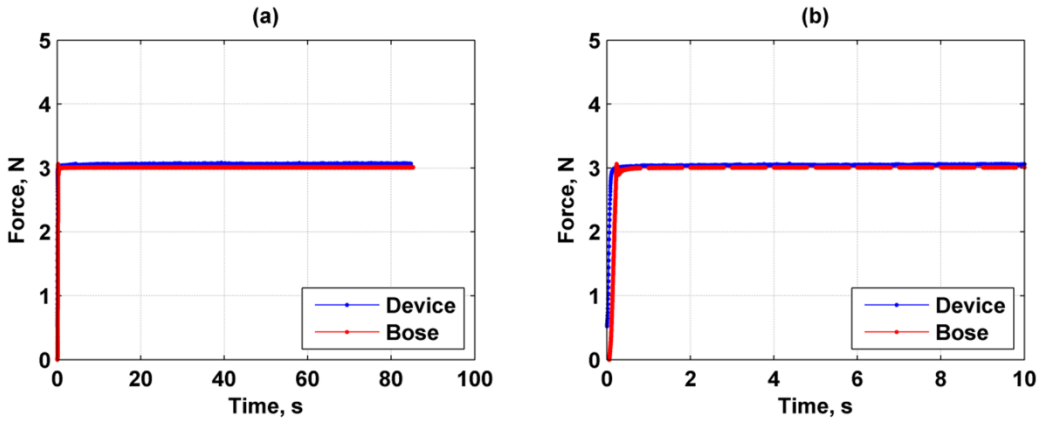

Figure 2.4 Comparison of Bose instrument and compression device in generating 3 N force with 18 N/s ramp. The ramp part takes 0.17 seconds and after that the force remains constant for 85 seconds. (a) Force profile for the entire 85 sec (b) Force profile for 10 seconds presented for better visualization.

2.3.1.2. Retardation Time Measurement

To validate the compression device performance, we measured the retardation time of a test phantom by the compression device and the Bose instrument and the outcomes were compared. For this purpose, we measured the surface displacement of the phantom.

Since the applied force is not a pure step function, the initial part of the response is a complicated mixture of the elastic and viscoelastic responses to the ramp excitation. However, after the force reaches its final value, it is safe to assume that the time varying part of the strain profile is only due to viscoelastic response. For this reason, the initial part of the response is excluded from the strain data analysis and the model is reduced to a second order Kelvin-Voigt model, Eq (2.5) [13, 23,51].

Figure 2.5 illustrates the surface displacement profile resulted from the Bose instrument and our compression device before and after fitting a curve according to Eq. (2.5). A nonlinear least square optimization method was used to find the closest fit to measure the two retardation times T_1 and T_2.

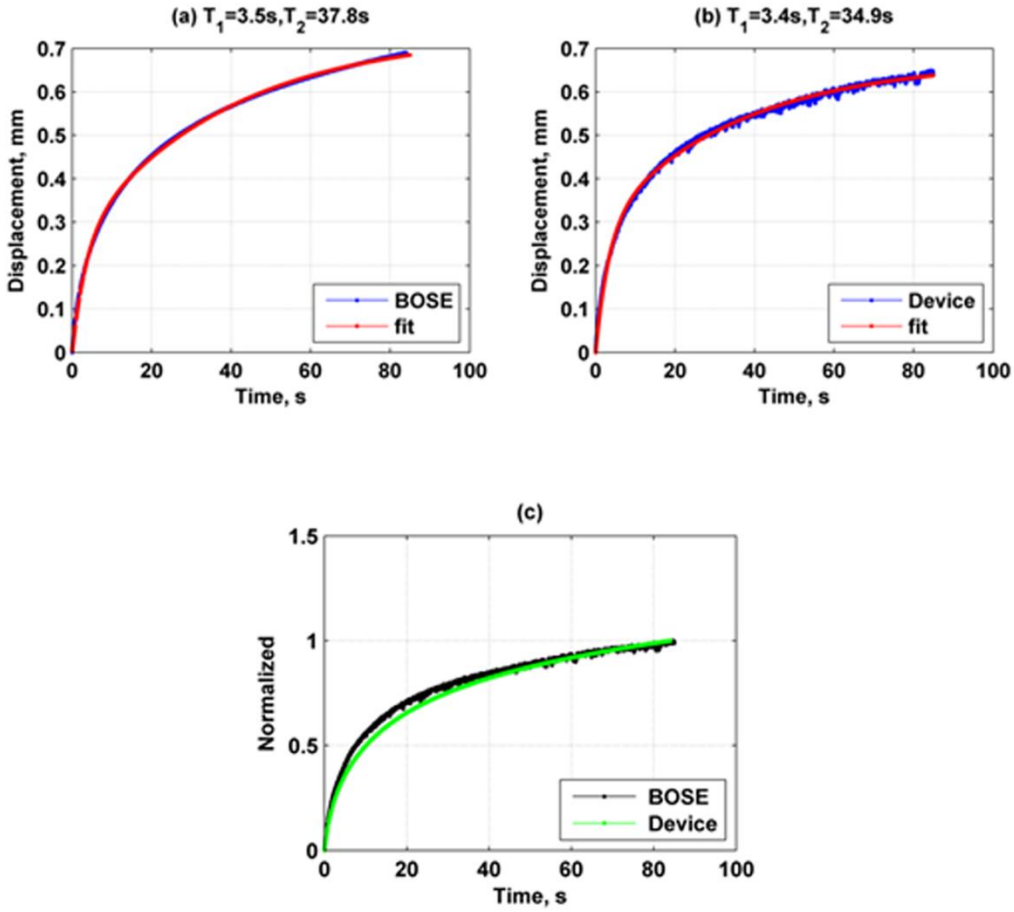

Figure2.5. Surface displacement profiles resulted from Bose instrument and the compression device. (a) Bose displacement profile and its fit with T_1 and T_2 value results. (b) Compression device displacement profile and its fit with T_1 and T_2 value results.(c) Bose and Device, normalized displacement profiles.

2.3.1.3. Curve fitting error

In order to evaluate the suitability of Kelvin-Voigt model for observed slow creep deformations, as shown in Eq. (2.5), it is necessary to quantify the amount of deviation from this model. The measured strain at a discrete time point t_n, n =1, N, can be modeled as

$$\hat{d}(t_n) = d_f(t_n) + e(t_n) \qquad (2.6)$$

where $\widehat{d}\,(t_n)$ is the measured strain and $d_f(t_n)$ represents the fitted viscoelastic compliance curve based on the selected model. The term $e(t_n)$ represents the residual error. A normalized error can then be introduced as expressed in Eq (2.7), where Q quantifies the goodness of the fit in terms of variance of the residual error, $\mathrm{e}(t_n)$, relative to the total measured strain variance

$$Q = \sqrt{\frac{\frac{\sum_{i=1}^{N}\left(\hat{d}(t_n) - d_f(t_n)\right)^2}{N}}{\frac{\sum_{i=1}^{N}\hat{d}(t_n)^2}{N}}} \qquad (2.7)$$

Such error measure has the advantage that model deviation can be quantified regardless of the total strain value.

Applying Eq. (2.7) on the displacement data in Figure 2.5 results in 0.52% error for Bose instrument response and 0.86% for the compression device response.

To test measurement reproducibility, we repeated these experiments five times on the same phantom using the same force, 3 N, and ramp speed, 18 N/s. Table I shows the resulting T_1 and T_2 values for these measurements.

Table 2.1 Retardation time results for five trials on the same phantom with the same amount of force and ramp speed for both the compression device and Bose instrument.

Measurement method	Retardation times T_1 and T_2 in seconds						
	First	Second	Third	Fourth	Fifth	Average	Standard deviation
BOSE T_1 (s)	3.4	3.4	3.5	3.5	3.4	3.44	0.05
Device T_1 (s)	3.6	3.2	3.4	3.2	3.4	3.32	0.17
BOSE T_2 (s)	37.5	39.8	37.8	37.4	37.3	37.96	1.04
Device T_2 (s)	33.8	31.8	34.9	32.4	33.8	33.34	1.24

In order to compare the results of two devices, a relative error for each parameter is defined as follows

$$E(\%) = \frac{T_D - T_B}{T_B} * 100 \qquad (2.8)$$

In this equation (T_D) is the retardation time, T_1 or T_2, measured by the compression device and (T_B) is corresponding values measured by the Bose machine which is regarded as the gold standard. Based on the average results of 5 trials, the percent error, *E(%)*, for T_1 and T_2 were - 3.49% and -12%, respectively. These results indicate a strong agreement between the creep device and Bose instrument.

2.3.2. Application of ultrasound in compression device:

In this section we present the application of the compression device combined with ultrasound strain imaging for viscoelasticity evaluation of a medium. The first step in retardation time imaging is acquiring in-phase/quadrature IQ data, analytic (complex) radiofrequency data, of the phantom that is being compressed by the compression device. Next, these data are used to calculate the strain at every pixel. Then the retardation time

at each pixel is estimated to produce an image depicting the retardation distribution across the phantom.

Figure 2.6 shows the block diagram of the ultrasound probe pressure plate and the location of the phantom

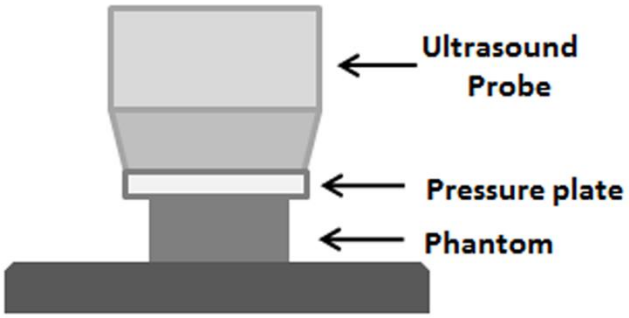

Figure 2.6 Block diagram showing the location of the probe, pressure plate and phantom which is located on a base

The phantom used for this experiment is the same one that was used in Section 2.3.1.1. We used the compression device to apply a 3 N force with 18 N/s ramp. A Verasonics ultrasound system (Verasonics, Inc., Kirkland, WA, USA) with a linear array transducer (L11-4v, Verasonics, Inc., Kirkland, WA, USA) was used to monitor the phantom response. For this purpose, we used plane wave mode [52] to acquire a series of IQ data of the phantom during the compression. Figure 2.7 shows the first B-mode image from the acquisition sequence. In this experiment, the ultrasound center frequency was 6.43 MHz and the frame rate was 20 Hz during the acquisition time of 85 seconds; thus 1700 frames were acquired.

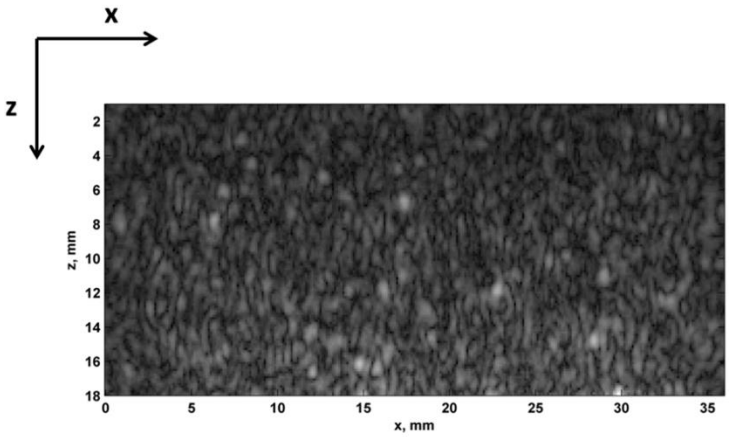

Figure 2.7 B-mode image of the homogenous phantom.

2.3.3. Displacement and strain calculation

A two-dimensional autocorrelation method was used to calculate the particle velocity from adjacent frames and then the displacements were estimated by integrating the particle velocity in time [30].

After calculating the displacement for all consecutive IQ data, the corresponding strain values were computed based on the gradient of the displacement. An axial 2-mm window was defined to measure the strain followed by a moving average filter with 1.2x1.2 mm size. The total strain map and the strain profiles are shown in Fig 2.8. Figure 2.8 (a) shows the spatial distribution of the total strain. Figure 2.8(b) depicts the strain profiles for the locations specified in 2.8(a). These curves were then normalized and shown in Fig. 2.8(c) where we also added the normalized surface displacement, which can be regarded as the overall strain behavior. As it can be seen the normalized strain profiles from different points show similar dynamics. It is also observed that the dynamic behaviors of these points closely match that of the normalized surface displacement, even though the total strain values are different. The spatial variations of the strain, as seen in Figs. 2.8 (a) and (b) are related to the geometry and the

boundary conditions of the medium, a phenomenon that has been discussed in many studies [53, 54, 55, 56].

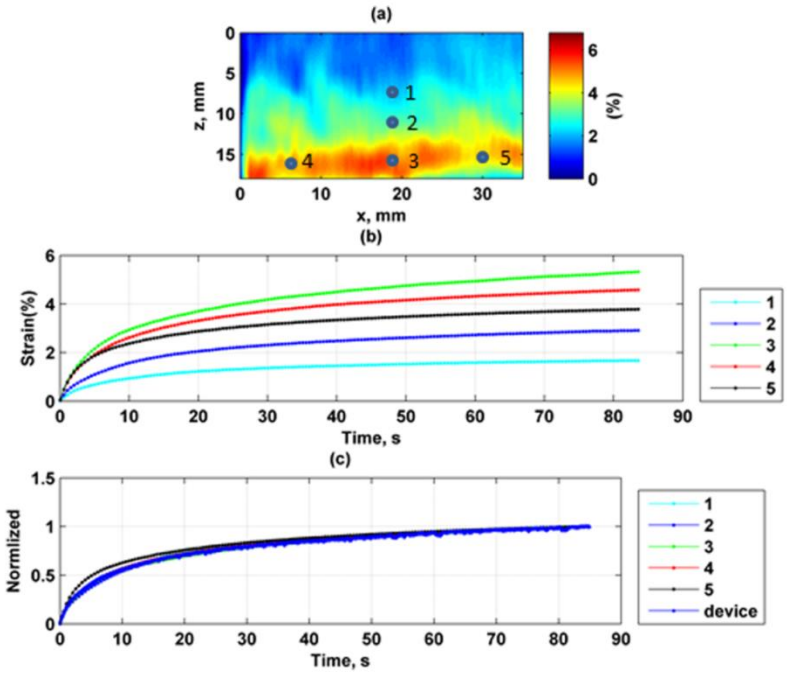

Figure 2.8 Strain results. (a) Strain map, (b) Strain profile for 85 seconds for 5 different spots specified in (a) strain map, (c) Normalized surface displacement obtained directly from the compression device and the normalized versions of the strain profiles shown in (a).

2.3.4. Retardation maps

So far, we have shown that how the viscoelastic properties of the material under creep test can be extracted using our device based on surface displacement and using a second order Kelvin-Voigt model. The same process has been executed for all the points within the strain map to calculate the retardation times, T_1 and T_2, based on their creep responses. Figure 2.9 shows the resulting T_1 and T_2 maps.

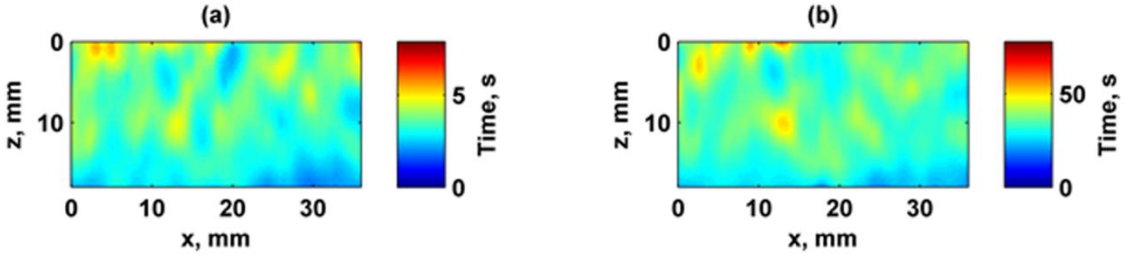

Figure 2.9 Retardation times maps based on creep tests on a homogenous phantom. (a) T_1 map (b) T_2 map.

The average values for these two maps in this figure are 3.4 seconds and 33.6 seconds for T_1 and T_2, respectively. It is also noted that compared to the strain map, Fig 2.8(a), the retardation time maps in Fig. 2.9, show a relatively uniform distribution with some scattered variation.

To evaluate the appropriateness of the second order Kelvin-Voigt model for this phantom, Eq. (2.7) was used for each pixel to form an error map shown in Figure 2.10. As it can be seen the error is mostly less than 2% which confirms that the suitability of the second-order Kelvin –Voigt model as well as the overall strain tracking performance.

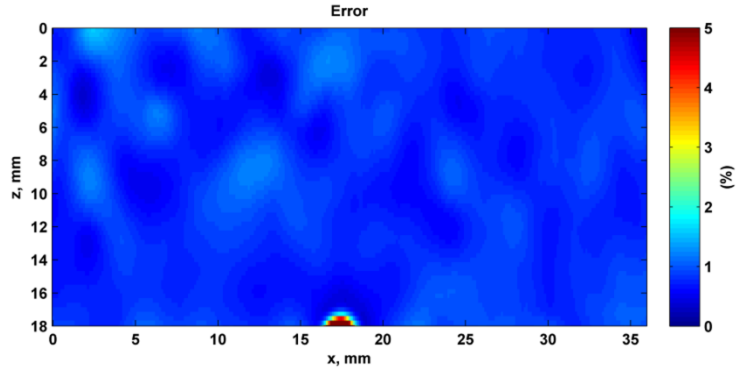

Figure 2.10 Fitting error for homogenous phantom

To explore the reproducibility of the results, this experiment was repeated 5 times on the same phantom with the same force, 3 N, and the ramp speed of

18 N/s. Table 2 shows the T_1 and T_2 values in 5 trials on the same homogenous phantom using the same force and ramp speed.

Table 2.2 T_1 and T_2 values

¤ Measurement method	Retardation time, T_1 and T_2 in seconds						
	First	Second	Third	Fourth	Fifth	Average	Standard deviation
US measurement: Mean T_1(s)	3.7	3.6	3.4	3.7	3.6	3.6	0.12
BOSE T_1 (s)	3.4	3.4	3.5	3.5	3.4	3.4	0.05
US measurement: Mean T_2(s)	32.4	32.0	33.6	33.0	34.0	33.0	0.74
BOSE T_2 (s)	37.5	39.8	37.8	37.4	37.3	38.0	1.04

The average T_1 and T_2 values measured with the Bose device were 3.4 s and 38 s, respectively. Comparing these values with those values measured by ultrasound and the average value of each T_1 and T_2 map is reported in Table 2.2, the resulting relative errors for T_1 and T_2 are 5.9 % and -13.1%, respectively.

2.4. Discussion

The goal of designing the automated compression device was to apply a prescribed amount of force for a predetermined time on a phantom or tissue to study its mechanical behavior or creep response during a period of time. The ultimate goal is to use this device for imaging the viscoelasticity of breast tissue in a group of patients.

One of the important elements in this device is the back and pressure plates that include four sensors located symmetrically at four corners of this plate. Outputs of these sensors are summed, thus these sensors collectively

measure the total applied force. Therefore, even in cases where the compression plate is not able to make complete contact with the surface of the object, for example, when the object's surface is not completely flat, the sensors can still measure the total force applied to the contact surface.

Another important design feature of this device is the location of the load cells or sensors. Being at the surface of the probe means that they can directly measure the force that is being applied to the medium, thus the mass and the inertia of the probe would not influence the force measurement.

The device ability to measure the force and the surface displacement profiles is another important feature. The surface displacement profile helps to validate this compression device with a standard mechanical machine like the Bose instrument.

To validate the compression device, the Bose instrument was used for comparison. Results showed strong agreements between the two devices with an average relative error of 3.49% and 12%, for T_1 and T_2, respectively based on surface displacement measured by these two devices.

Furthermore, investigation to measure retardation times for each point inside the same phantom by ultrasound reveal a good agreement between the surface and internal computed retardation time constants where the error was less than 15 % totally.

We also showed that the measured retardation times T_1 and T_2 across a uniform phantom resulted in relatively uniform maps as shown in Figure 2.9. This can indicate that compared to the total strain, these parameters are less sensitive to the geometry and boundary condition variation

Appropriateness of a second order Kelvin-Voigt model was tested. Figure 2.10 showed that the fitting error was less than 2% in most of the region

across the phantom. Reproducibility tests also showed that the retardation times could be measured with small variations in measurement results.

Future work will include using the automated compression device described here to measure the retardation time in human breast for diagnostic purposes.

2.5 Conclusion

In this Chapter we described the design of a device for applying an approximate step force on a tissue mimicking phantom and measuring the creep response using an ultrasound probe. Device performance was validated against a standard mechanical testing instrument by enforcing a second order Kelvin-Voigt model on the displacement profiles from both devices. The device was validated through a series of creep tests on a phantom and comparing the results retardation times with those from a commercial mechanical testing device.

Using ultrasound imaging capability of the device, internal strain was computed and retardation times T_1 and T_2 were acquired, showing strong agreement with those of surface displacement measurement tests.

The overall results of this work justify the suitability of this device for performing creep tests on tissue-like materials.

2.6 Contribution:

- Validating the new device based on the standard mechanical instrument
- Making Visco elastic phantom with gelatin and Vanicream to show the contrast based on the retardation time measurement.

Chapter 3

Automated Compression Device and its reproducible performance in measuring retardation time in different viscoelastic media

Introduction:

Ultrasound elastography is an imaging modality that maps local strain, based on the pre- and post-compression effects on a medium. An elastogram or strain map reports the result of applying a spatial gradient on the displacement measurement of each point in post-compressed medium by comparing to pre-compressed one [11].

One of the methods that consider the strain behavior of medium during the compression time is called creep test. In this method, a step-force excitation is applied, and the subsequent transient response based on the viscoelastic properties of the medium is estimated. Fitting the Kelvin-Voigt model to this transient response and measuring the retardation time, T_1, is a common method to evaluate the transient response of a medium and its viscoelastic properties [13, 14, 38, 57].

Several devices have been designed to apply force on the medium with an ultrasound probe. Such a configuration can add the ability of recording a sequence of ultrasound radiofrequency (RF) data through the compression period to provide a temporal displacement profile for each point in different organs like prostate [44], skin [45] and vessels [46] but there is a major difference; some of the devices are fully automatic [25, 48], while manual assistance is needed for the others [42, 43, 58].

Although the *in-vivo* creep response was studied initially by hand-held compression [14], it may be preferred to apply a device to better control the step-force stimulus to increase the chance of repeatability and

reproducibility of the generated data, especially when the study involves a large group of patients.

In the previous Chapter we described the design and validation process of a compression ultrasound device and its application, as well as the algorithm to measure the strain and T_1 value. A retardation time map, T_1, in a uniform phantom was also shown.

The goals of this Chapter is first to demonstrate the repeatability and reproducibility of compression device performance on various phantoms and then testing the performance and applicability of Automated Compression Device for differentiating between malignant and benign breast tumors in an in-vivo study.

3.1. Application

3.1.1 Phantom study:

There is no standard device to measure the intrinsic retardation time, T_1, value of tissue. Thus to evaluate the performance accuracy of the compression ultrasound device, we chose to repeat the experiment four times on each different phantom sample, to check for repeatability and reproducibility of the outcomes. We built two uniform cubic phantoms, one stiff and the other soft. We created a third inclusion phantom in which the background material was similar to the soft cubic phantom, and the cylindrical inclusion was made from the same material as the stiff cubic phantom.

The cubic phantom dimensions are 7.5 cm x 5.5 cm x 2 cm (L x W x H) for both. The inclusion phantom dimensions are 7.5cm x 5.5cm x 5.5 cm (L x W x H), with the cylindrical inclusion having a 1.5 cm diameter.

The stiff phantom is made of 25.14 grams of gelatin (Sigma-Aldrich; St. Louis, MO); 60 ml of propylene glycol (Sigma-Aldrich, St. Louis, MO); and 4 grams of cellulose (Sigma-Aldrich) for ultrasound scattering, dissolved in enough distilled water to make the total solution volume equal 300 ml. For the soft phantom we used 32.3 grams of gelatin (Sigma-Aldrich, St. Louis, MO); 30 ml of Vanicream Lite (Pharmaceutical Specialties, Inc., Rochester, MN); 6 grams of cellulose (Sigma-Aldrich) for ultrasound scattering; and 6 grams of potassium sorbate (Sigma-Aldrich) as a preservative, dissolved in enough distilled water to make the total solution volume equal 600 ml.

In Chapter 2, we described the design and validation process of this compression device. The same device has been applied to carry out the experiments in this paper. This device applies constant stress to the phantom after a short ramp and measures the continuous deformation of tissue under constant stress by means of its ultrasound probe. This device also provides force and surface displacement profiles. These features of the device are useful to validate and extract the viscoelastic response of the resulting creep curve.

To measure the dynamic response of the medium, we used the compression device to apply 8 N force with 16 N/s ramp on each of the phantoms. Then to monitor the phantom response, a Verasonics ultrasound system (Verasonics, Inc., Kirkland, WA, USA) with a linear array transducer (L11-4v, Verasonics, Inc., Kirkland, WA, USA) was used. The plane wave imaging [52] mode of this system was employed to acquire a series of B-mode images of the phantom during compression. The ultrasound center frequency was 6.43 MHz. The frame rate was 20 Hz during the acquisition

time of 20 seconds; thus 400 frames were acquired for each of the phantom experiments.

In order to reduce memory needs and processing time for the inclusion phantom, we considered approximately 3 cm of B-mode images in the axial direction, and for uniform cubic phantoms, we considered only 1.8 cm of B-mode images. All of these experiments were done at room temperature.

We ignored the initial two seconds of data to ensure that the force had reached to steady state and the viscoelastic part of the creep response had been started.

To measure the intrinsic strain profile, we used the same algorithm applied in the previous Chapter except we increased the spatial differentiator length from 20 λ to 40λ to have better estimation of strain [59].

Figure 3.1(a) illustrates B-mode image of inclusion phantom with some specified points. Figure 3.1(b) shows strain behavior of these specified points through time. Point 1 and 2 are inside the inclusion and points 3 and 4 are outside. As the inclusion is stiffer than the background, it demonstrates less strain than the background. In Figure 3.1(c) the normalized force profile after truncating two initial seconds is added to the strain profiles after they are normalized.

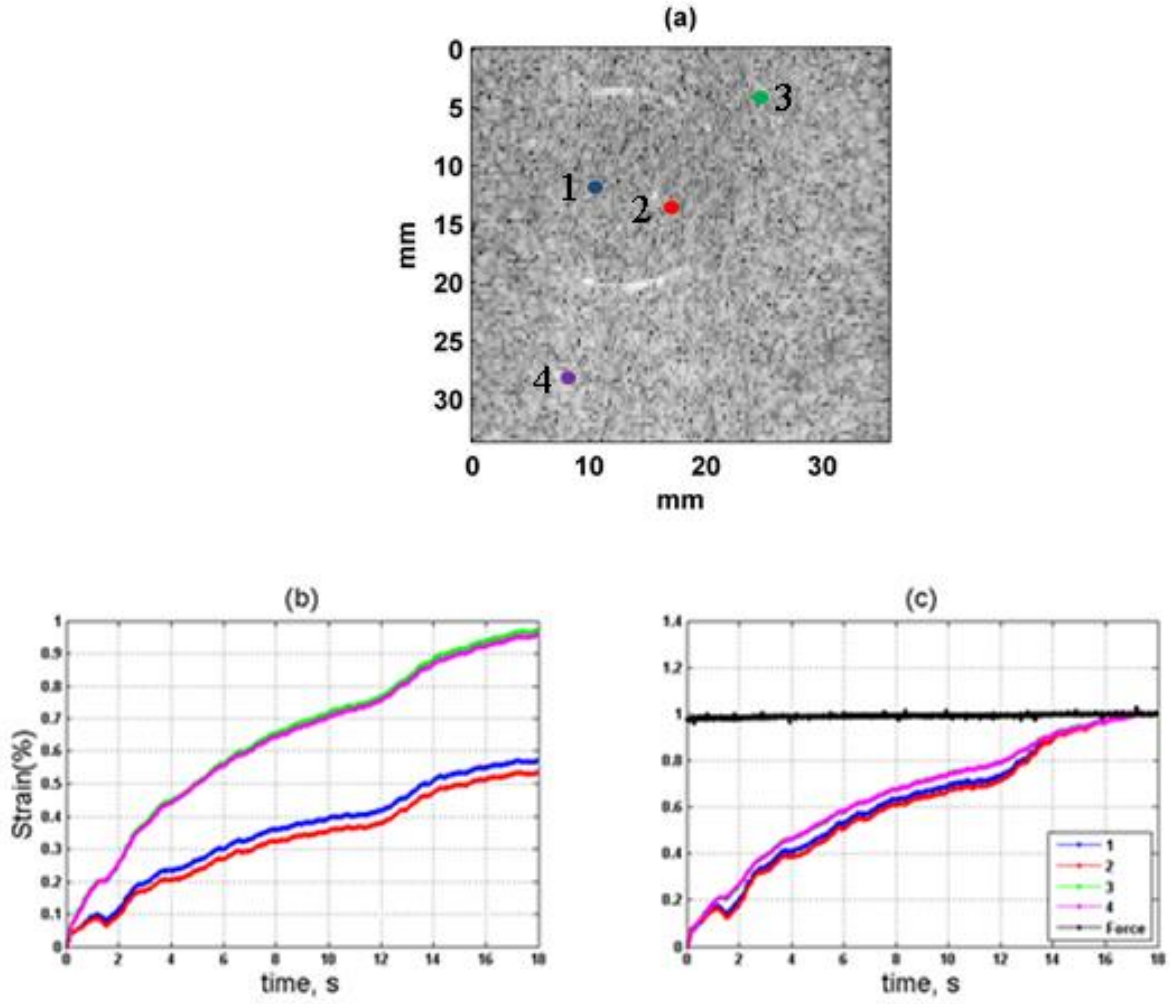

Figure 3.1 B-mode and strain profiles. (a) Last B-mode image (b) strain profiles of different locations specified in B-mode image (c) normalized strain profiles accompanied with force after cutting two initial seconds.

The same procedure tests the rest of the phantoms, and Figure3.2 shows the strain map results for all these cases. The strain maps in this figure show the outcome of the creep response after cutting the initial 2 seconds of data.

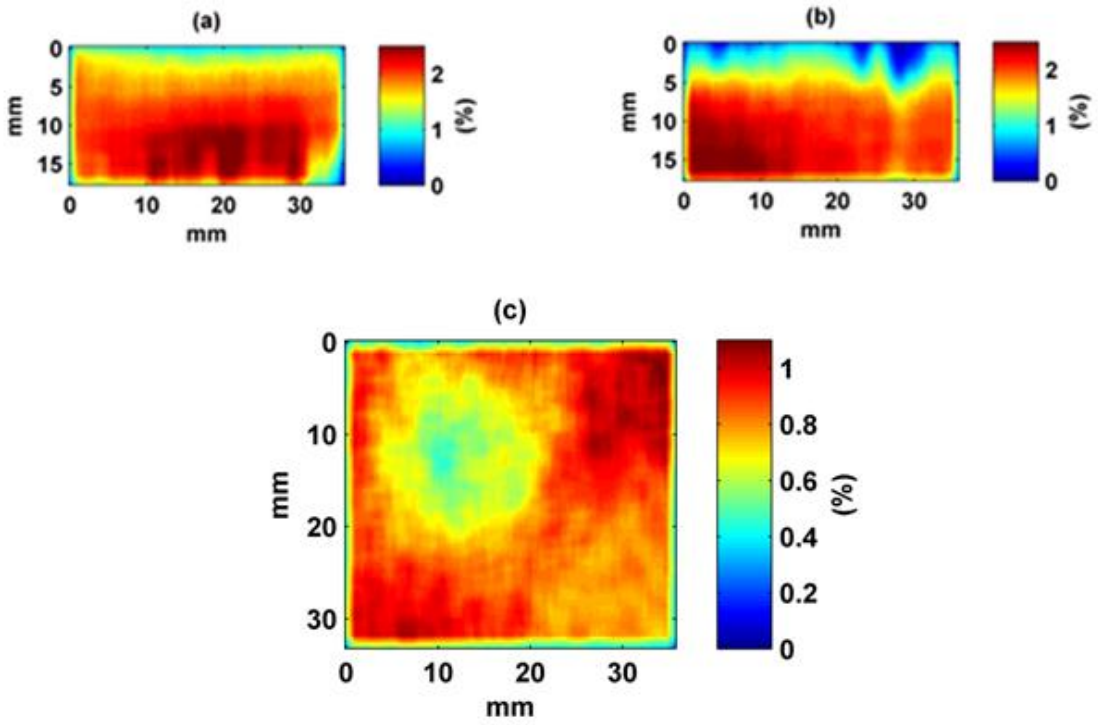

Figure 3.2- Strain maps (a) Strain map in a cubic soft phantom (b) Strain map in a cubic stiff phantom (c) Strain map in an inclusion phantom.

3.2 Retardation Time Measurement and Map:

As explained in the previous Chapter, acquiring the strain profile can help to measure the retardation time, T_1, for each strain profile. A nonlinear least squares optimization method was used to measure the T_1 value for each temporal strain profile. The map was created based on this procedure.

To quantify and compare the T_1 value for all cases, we calculated the mean of the specified, black-dashed rectangle and blue circle for background and inclusion and show results in Figure 3.3. These values are reported in Table 3.1.

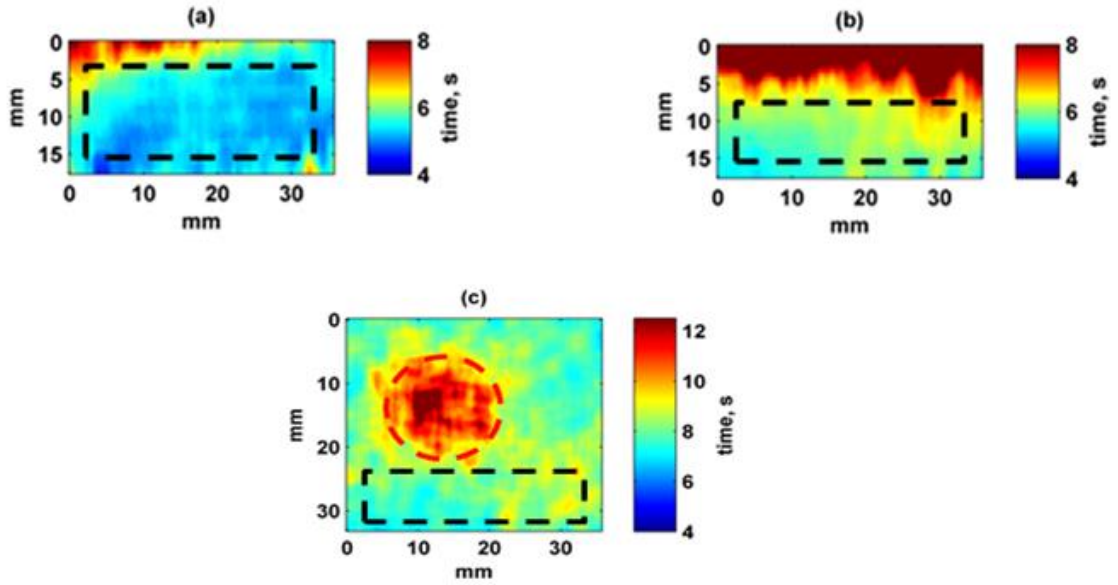

Figure 3.3 T_1 maps. (a) T_1 map for cubic soft phantom. (b) T_1 map for cubic stiff phantom. (c) T_1 map for phantom inclusion. The black dashed rectangle represents the area that has been considered for measuring T_1 value. In phantom inclusion, the red-circle shows the area to measure T_1 value for inclusion.

In Figure 3.3(a), the black rectangular specified region for the soft phantom is noticeably larger than that of the stiff phantom, Figure 3.3(b).

This is because the amount of strain is different for these two different phantoms under the same force with same ramp, as has been mentioned in earlier discussion about the strain images. We tried to find the region that shows enough strain and reliable time constant value in both cases, which makes it possible to compare them.

Error fit maps in Figure 3.4 illustrate the performance of the fitting function. In this figure, the error rate is less than 5% for both the soft and stiff uniform phantoms, but the part close to the probe shows higher error and covers some area on top, Figure 3.4(b).

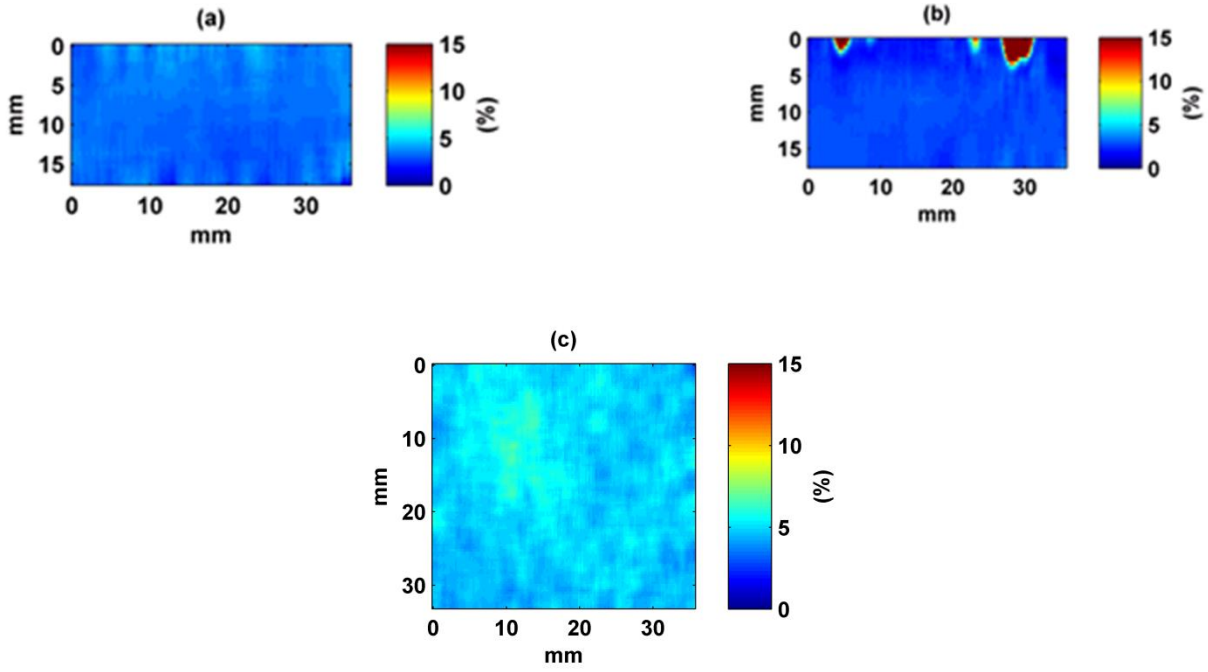

Figure 3.4 Fitting residue maps. (a) Fitting residue map for soft phantom. (b) Fitting residue map for stiff phantom. (c) Fitting residue map for phantom inclusion.

The calculated error for the inclusion phantom, for the background and inclusion part, was less than 8%, Figure 3.4(c), which means the points in these parts predominantly follow the Voigt model.

This experiment was repeated four times for each case. Each experiment involved an equal amount of preload and a delay of almost 5 minutes between each trial, without any change in the position of the phantom. The T_1 value has been reported in Table 3.1. To measure the T_1 value for background and inclusion, an area has been specified in Figure 3.3(c), and the reported T_1 is the mean value of these specified regions.

We measured the Coefficient of variation, COV in Eq.(3.1):

$$COV = \frac{\mu}{\sigma} * 100 \qquad (3.1)$$

In this equation, μ is the average value and σ is the standard deviation.

Table 3.1 T_1 values for cubic block phantoms

Retardation time	Cubic block phantoms						
T_1 (sec)	First	Second	Third	Fourth	Average	Std	COV(%)
Stiff	7.1	7.9	7.4	6.7	7.0	0.8	11.4
Soft	5.9	5.5	5.8	6.3	5.8	0.5	8.6

As Table 3.1 demonstrates, after applying several equivalent creep tests on two different cubic phantoms, T_1 values are almost the same with low standard deviation, which confirms the repeatability of our device performance. And the same process is performed for inclusion phantom. Table 3.2 shows the measured T_1 values for inclusion and background part of this phantom after 4 trials.

Table 3.2 T_1 values for Inclusion phantom

Retardation time	Inclusion phantom						
T_1 (sec)	First	Second	Third	Fourth	Average	Std	COV(%)
Inclusion	9.1	10.3	9.1	10.4	9.7	0.7	7.2
Background	7.2	8.0	7.0	7.3	7.4	0.4	5.4

Comparison between Tables 3.1 and 3.2 reveals a noticeable point that the average values for T_1 related to stiff cubic phantom and inclusion in inclusion phantom are not the same, even if they are made from the same materials. The same condition happens for soft cubic phantom and background in inclusion phantom, which means that this value can depend on shape, geometry and boundary conditions; however, when it comes to the contrast, it is almost the same. For stiff and soft uniform cubic phantom, the contrast is 1.2; and for the inclusion part and the background part in the inclusion phantom, the contrast is 1.3.but this claim needs more investigation and phantom study to see the role of the geometry ,shape and boundary condition on T_1 measurement and its ratio.

The maximum Coefficient of Variation value, COV, reported in Table 3.1 and 3.2 is less than 12%, which indicates a good agreement for measuring T_1 value for each trial. However, ideally these values are supposed to be the same.

3.3 Patient Study:

The main goal for this study is to employ the Automated Compressional Device for a large group of patients in the future.

We conducted a study on two patients, one with a benign, fibroadenoma, and one with a malignant tumor, to evaluate the device's performance. The force was 2N with 8 N/s ramp. We used the same ultrasound probe, but the frame rate was 200 frames per second. We asked the patient to hold her breath for nearly 10 seconds while recording the data. The initial one second of patient data was excluded to be sure the force had reached its steady state.

Figure 3.5(a) depicts the B-mode image of the benign breast patient. The final retardation time map, T_1, is shown in Figure 3.5(b) which is registered on the B-mode image to better specify the tumor boundaries. As is clear in this registered map, Fig. 3.5(b), the T_1 value for benign tumor is between 2.5 and 3 seconds while for the back ground it is between 1 and 2 seconds. In the benign case the T_1 value of tumor part is higher than back-ground tissue [14].

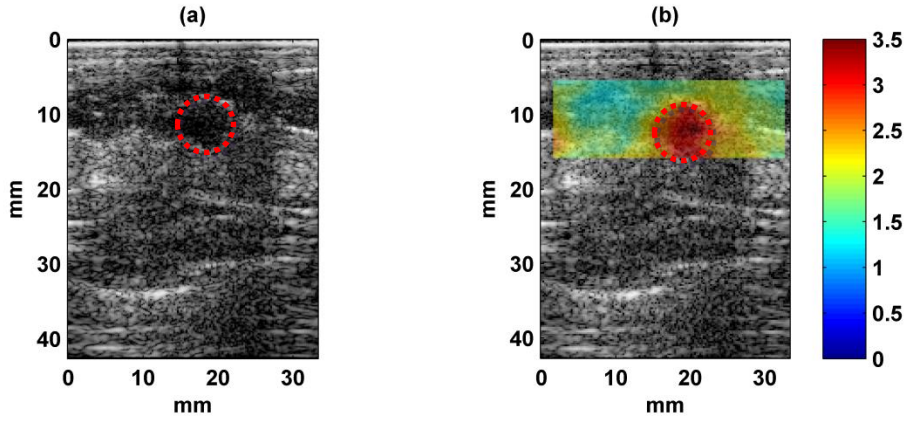

Figure 3.5 (a) B-mode image of benign patient; red circle specifies the benign lesion location. (b) Registered retardation T_1 map on B-mode image.

We performed the same procedure for the malignant case. Figure 3.6 shows the B-mode image. The T_1 map is registered to the B-mode image in Figure 3.6(b). The blue area in this map belongs to malignant tumor.

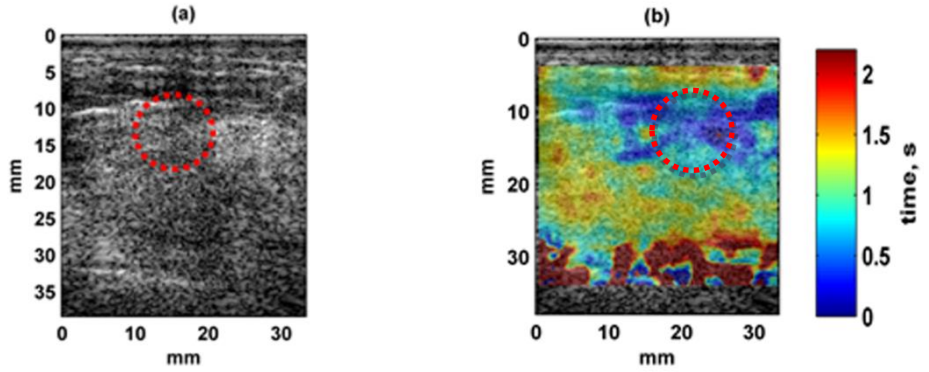

Figure 3.6 (a) B-mode image of malignant patient; red circle specifies the benign lesion location. (b) Registered retardation T_1 map on B-mode image.

Figure 3.6(b) shows the T_1 value for the malignant tumor is between 0 and 0.5 second and for the background is between 0.8 and 1.5 seconds. In contrast with the benign case, in malignant tumor the T_1 value is lower than background tissue [14].

3.4 Discussion:

The purpose of this study was to evaluate the repeatability of Automated Compression Device performance. To the best of our knowledge, there is no standard mechanical instrument with ability to measure the local strain or creep response of the medium internally and locally with which we could compare the performance of our device. It is possible to repeat measurements using this device on different media to assess its repeatability performance.

The long-term goal for designing this device is its usage for a large group of breast patients. Gelatin is an appropriate model to study the viscoelastic properties of breast tissue because of its similarity to breast stroma [23]. In both of them the mechanical properties are established by a high molecular-weight, type I collagen matrix that is saturated in water [23]. However, it should be noted that the thermal and mechanical sensitivity of living stroma

compared to gelatin phantom, is considerably less. According to the similar viscoelastic spectra of two media, it is reasonable to assume that gelatin is the most appropriate model for developing the viscoelastic breast technique [23].

Figure 3.5 and Table 3.1 showed that increasing the gelatin concentration caused the retardation time to increase [13]. As was observed, generally the cubic stiff phantom had a higher T_1 value compared to the soft one, and likewise the inclusion in the inclusion phantom had a higher value than the background part in this phantom.

Both of the cubic phantoms were uniform phantoms and supposed to have a uniform strain, but in practice some non-uniformity is observed in these maps that occurs due to either inconsistent distribution of the force in medium [23] or the strain calculation algorithm which considers the axial displacement not lateral displacement [53, 54, 55, 56].

Although there is at least a 5 minute interval after each compression, this resting time may not be sufficient for the phantom to come back to its initial position, and its memory due to previous compression may cause error. Temperature could be another factor for this discrepancy; dehydration could possibly cause this inconsistency [61].

In patient studies we cannot wait more than 5 minutes between each set of data [25].

From the material science point of view, the huge heterogeneity and undetermined microstructure of the breast make the accurate measurement of the intrinsic mechanical properties of this medium difficult or almost unfeasible because the accuracy of material property measurements depends on sample geometry, boundary conditions, and spatial distribution of applied mechanical stimulus [33]. In other words, we are struggling to approximate

the viscoelastic properties of a medium which depends on shape and alignment of unknown inner structures that hardly can be sensed by ultrasound in detail [33]. Thus the accurate measurement of such properties seems impossible, but controlling the force and ramp part by a fully automatic device and increasing the surface contact of the probe by employing a pressure plate to distribute the stress more evenly through the breast tissue can partially alleviate some of the aforementioned problems however, it is not still possible to measure the mechanical property of tissue quantitatively.

A larger compression surface enhances uniaxial creep stress and closed-loop force control improves stress stability during creep observation which is a requirement for this type of mechanical testing. In spite of all inaccuracy, initial patient studies are promising and it is expected that markers based on creep test can be used an accurate breast tumor classifier.

Qiu *et al.* [14] showed that retardation time ,T_1 value, in benign tumor is higher than malignant cases. We did creep tests with the automated compression device on two different patients with benign and malignat tumor. Figure 3.5 (b) and 3.6 (b) confirmed the shorter retardation time in malignant case compared to benign one [14]. The main difference in this study is that the creep tests were done by a fully automated compression device with ability to control the force amplitude and its speed ramp part for both subjects. Another unique point of this study

was its reccording frame rate which was alsmost 10 times more than the previous *in-vivo* study. This capability can capture the motion more accurately and decrease the decorrelation that can occur due to low fram rate.

3.5 Conclusion

In this Chapter the repeatability of the Automated Compression Device was examined by executing the same amount of force and ramp on different viscoelastic phantoms and repeating that process for each of them four times.

These tests confirmed that this device, which is capable of tracking the creep response of the medium internally and locally, can produce reliable results at least from the reproducibility point of view.

After this step, we checked the device application on patient and its suitability for breast patient study. Our primary results of patient study were almost similar to other patient study [14] with a completely different mechanism of applying force.

3.6 Contributions

- Demonstrating the repeatability of automated control device on three different gel phantoms: uniform stiff phantom, uniform soft phantom and inclusion phantom
- Applying the automated compression device on patients. and constructing the T_1 map based on recorded *in-vivo* data for both malignant and benign lesions.

Chapter 4.

Phase difference between relative loss and storage modulus of local creep response for viscoelastic medium in sub-Hertz frequency range.

Introduction

The ultrasonic creep test has the ability to assess the viscoelastic mechanical properties of tissue intrinsically and noninvasively. Applying a step-force and monitoring the local viscoelastic strain response ultrasonically are the two main components of this method. In other words in this method a step-force is used as stimulus, and the transient strain response, which is governed by viscoelastic properties of the medium, is monitored by recording a sequence of radiofrequency (RF) data during the excitation [13,14].

The ultrasonic creep test can be divided into two major branches internal and external tests, based on the excitation. In the internal ultrasonic creep test acoustic radiation force is employed to apply a step force which is local and occurs inside the medium without any changes in boundary condition, geometry and shape while exciting the medium [20, 22, 61]. In the external ultrasonic creep test a quasi-static stimulus is applied to the entire medium by ultrasound probe. The probe motion is driven either manually or automatically [13, 14] for a predetermined time with no contribution of acoustic radiation force.

The external ultrasound creep test is more common than the internal one and can be considered as the new generation of elastography method in which rather than the elasticity the viscoelastic properties of the medium are studied [13,14].

Fitting the multi-exponential creep curves to a low-order discrete Voigt model to estimate the retardation times is a common method to quantify the viscoelastic creep behavior of the medium in time domain [13, 14]. However, it is possible to calculate the viscoelastic properties of time-dependent creep response in the frequency domain. Evans *et al.* [32] came up with a formula that converts time-domain creep compliance to frequency-domain complex modulus in a model-independent way.

Later this method was used by Amador *et al.* [20] to quantify viscoelastic properties by estimating the complex elastic modulus and loss tangent from time-dependent creep responses induced by acoustic radiation force.

The loss tangent is the ratio of the imaginary component of the complex modulus to the real component [63]. The imaginary part of the complex modulus is called the loss modulus and the real part is the storage modulus.

The loss modulus indicates the dissipation of energy in the medium whereas the storage modulus represents the stored energy in the system while applying force or stress. Hence, the storage modulus defines the elastic deformations under stress and loss modulus describes the viscous deformation [64].

A smaller loss tangent is related to more elastic medium while a medium that absorbs energy through viscous processes has a higher loss tangent [65]. Consequently the loss tangent can be a good candidate for evaluating the viscoelastic response of the medium in the spectral domain.

Applying a standard mechanical device to measure either the complex compliance [63] or storage and loss parameters or its ratio as loss tangent is common. Generally, in these standard mechanical devices an oscillating stress with different frequency ranges is applied and the strain response at each frequency is detected. By measuring the phase difference between the

stress as stimulus and strain as the response it is possible to quantify the loss tangent at different frequency range. Although these standard devices can measure the loss tangent in a very accurate ways, it is impossible to use them for *in vivo* study and for measuring the loss tangent locally in the medium. For all of these standard mechanical devices the sample size and the geometry are important factors and the measurement is mostly based on the surface displacement or surface strain of sample not the displacement or strain inside it. This is the reason that all the studies that have been done so far focused on a sample of tissue and performed *in vitro* [63].

Several studies either directly or indirectly confirm that the viscous contribution in lower frequency ranges of viscoelastic response is superior to the higher frequency range [38, 66, 69], especially when it comes to creep response spectrum which cover a wide range of frequencies depending on the initial rising part of temporal creep response, or the speed ramp part of the creep response which determines the high frequency ranges of creep response depending on how fast the ramp speed happens for our study is less than 4Hz if the applied force is 2 N and ramp speed is 8 N/s . The whole duration of the creep response will determine the low frequency ranges of creep response that are more than 0.05 Hz if the creep response takes 20 seconds [32].

This is the main reason that motivates us to focus on low frequency components of the creep spectra to study the viscous component effect on contrast in loss tangent map created in frequency range less than 0.3 Hz. In addition, in this range of frequencies the spectrum is less noisy than within higher frequency ranges [38, 63] and also the effect of the ramp part of the force stimulus in external ultrasonic creep test is minimal on spectral creep estimation at low frequencies, less than 0.3 Hz [13].

The essential part of this Chapter is based on computing the phase difference, between the storage and loss modulus by applying the Evans method [20, 32] on the local time-dependent creep response, It is necessary to validate this method with a standard model like Kelvin-Voigt in terms of measuring δ in low frequency range.

The first part of this Chapter is devoted to comparing these two methods based on simulation. The remainder of this Chapter is organized as follows. In section one, we provide an overview for two different methods; model based and model free, to measure δ. In section two, we use the simulation to check the validity of model -free methods according to model-based method for computing δ. In section three the model free method is used on phantom data and the results are shown. In the last section of this paper we discussed the advantages of model-free methods over model-based ones. This Chapter concludes with a summary of the results and ongoing future work of this introduced method.

4.1. Methods:

4.1.1 Retardation time:

The viscoelastic material stress response is related to both the strain and strain rate [68]. The Kelvin-Voigt model can represent this behavior through Eq. 4.1

$$\sigma(t) = E\epsilon(t) + \eta \frac{d\epsilon(t)}{dt} \qquad (4.1)$$

where E is the material's elasticity and η is the viscosity parameter. By applying a sudden constant stress, σ_0 on Kelvin-Voigt material the response can be described by Eq.4.2.

$$\epsilon(t) = \frac{\sigma_0}{E}\left(1 - e^{\frac{-t}{T_1}}\right) \quad (4.2)$$

In this equation T_1 is defined as

$$T_1 = \frac{\eta}{E} \quad (4.3)$$

The T_1 value is related to the viscosity and elasticity of the viscoelastic medium [13,14].

Applying the Laplace transform on Eq. (4.2) makes it possible to extract the real and imaginary parts in the spectral domain which are called storage and loss moduli, respectively [20]. The complex dynamic modulus of Kelvin-Voigt materials is given by:

$$E^* = E + i\eta\omega \quad (4.4)$$

The magnitude of the complex dynamic modulus, M, can be defined as:

$$M = \sqrt{E^2 + (\eta\omega)^2} \quad (4.5)$$

The ratio between the imaginary and real parts of the complex dynamic modulus is the loss tangent or *tan (δ)* as explained in the previous Chapter [20, 63].

$$\tan(\delta) = \frac{\eta\omega}{E} \quad (4.6)$$

Thus the phase difference, δ, is equal to:

$$\delta = \arctan\left(\frac{\eta\omega}{E}\right) \quad (4.7)$$

4.1.2 Evans' method and δ measurement:

The loss tangent can be used in evaluating the viscoelastic response of the medium [20]. Considering the local creep response of the medium and assessing the loss tangent based on applying Evans' method is the main goal of this study. Amador *et al*.[20] demonstrated that Eq.(4.8) can be used to

convert the time-dependent compliance, $J(t)$, to complex shear modulus, $G(\omega)$:

$$G^*(\omega) = \frac{i\omega}{i\omega J(0) + \frac{e^{-i\omega t(N)}}{\eta} + \sum_{n=1}^{N}\left(\frac{J(n)-J(n-1)}{t(n)-t(n-1)}\right)\left(e^{-i\omega t(n-1)} - e^{-i\omega t(n)}\right)}, \quad n = 1{:}N \tag{4.8}$$

where n is time sample index, J(0) is the compliance at n=0 which is estimated by extrapolation of the compliance function to t $\rightarrow$ 0.The parameter η represents the steady state viscosity which is estimated by extrapolation of compliance function to t$\rightarrow \infty$.

The unique characteristic of this equation is its independence of fitting the theoretical model to convert time-dependent compliance, J(t), to the complex shear modulus, $G^*(\omega)$

$$\tan(\delta) = \frac{G_l(\omega)}{G_s(\omega)} \tag{4.9}$$

where $G_l(\omega)$ and $G_s(\omega)$ are the imaginary and the real parts of the complex shear modulus illustrated in Eq.(4.8).

Thus the δ is equal to

$$\delta = \arctan\left(\frac{G_l(\omega)}{G_s(\omega)}\right) \tag{4.10}$$

One of the important aspects of measuring loss tangent and δ in either internal or external ultrasonic creep test is that despite the storage and loss modulus, the δ and loss tangent are independent of the stress distribution in the medium [20, 69].

4.2 Simulation:

In order to assess the performance of Evans' method we performed simulation based on one exponential creep response, Eq. (4.2) and compared the δ results for both the analytical methods, Eq.(4. 7), and the Evans method, Eq.(4. 10).

It should be noted that the analytical method that has been described is based on the one exponential Kelvin-Voigt model, Eq.(4.2). As we have shown in the previous Chapter in both the phantom study and patient study, the creep response followed a single exponential creep response. In the worst case the residual fitting error was less than 15% [14].

So the first order single exponential response could be a good benchmark for assessing Evans' method in model-free methods.

4.2.1 Simulations

We simulated the time-dependent creep response as one exponential Kelvin-Voigt model. Equation (4.2) is the input for all the simulation cases. In this equation the amplitude is the ratio of the stress over strain, $\frac{\sigma_0}{\epsilon}$, and for all the simulation cases we assume that the $\sigma_0 = 1\ Pa$. In the following figures the analytical part is denoted as, Ana, and is compared with Evans' method denoted as, Ev.

Figure.4.1 shows the effects of the amplitude, A= $\frac{\sigma_0}{E}$, and T_1 values in Eq. 4.2 on, δ in frequency range less than 0.4 Hz.

The first row in Figure 4.1 shows the results based on the same T_1 values but different amplitude .As shown in Fig 4.1(b), both the δ resulting from the analytical method and Evans' method are in agreement and the variation in amplitude does not affect the δ profile. In the second row of this figure the

amplitudes of input are the same, but T_1 values have been changed. Again the δ profiles of both methods have the same trend in this range of frequency but the model with higher T_1 value has a higher δ compared with the one with the lower T_1 value.

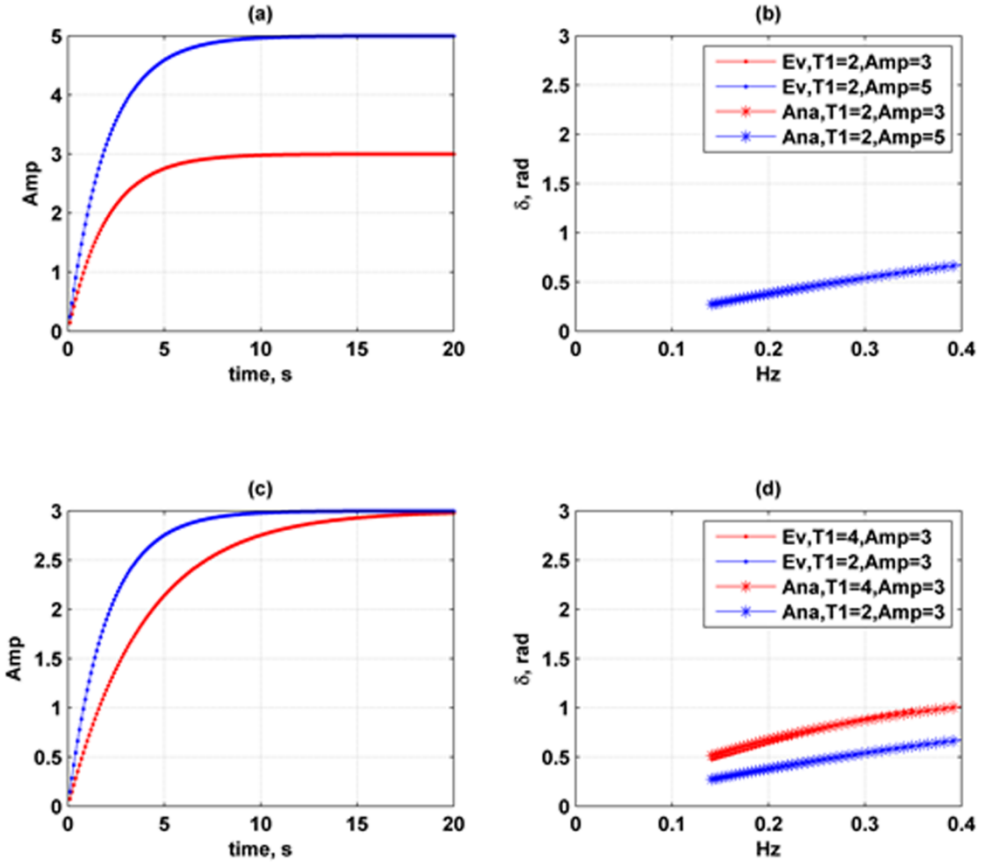

Figure.4.1 Comparing δ behavior due to difference in amplitude, A, and T_1 values for equation 2 as an input. (a) Inputs with same T_1 value and different amplitudes (b) resulted δ profiles (c) Inputs with same amplitudes and different T_1 values (d) resulted δ profiles

4.3 Phantom study:

4.3.1 Uniform phantom:

Simulation results in the previous section showed that the δ behavior resulting from Kelvin-Voigt model, Eq.(4.7) and Evans method, Eqs. (4.8-

4.10), corroborated well in low frequency ranges, less than 0.4 Hz. To validate Evans' method on a phantom we applied the same soft uniform phantom data used in previous Chapter. Figure 4.3 demonstrates the T_1 map, Figure 4.2(a), and it's fitting error map, Figure 4.3(b), using Eq. (2.7). accompanied with the strain profile of one point specified in Figure 4.2 (a) with its fitted curve, Figure 4.2 (c). In Figure 4.3 (d) the resultant loss angle profile, δ, of applying Evans methods on strain data of specified point in Figure 4.2 (a), blue curve, accompanied by applying Evans' method on fitted curve, red curve, and also analytical method on fitted curve, green curve.

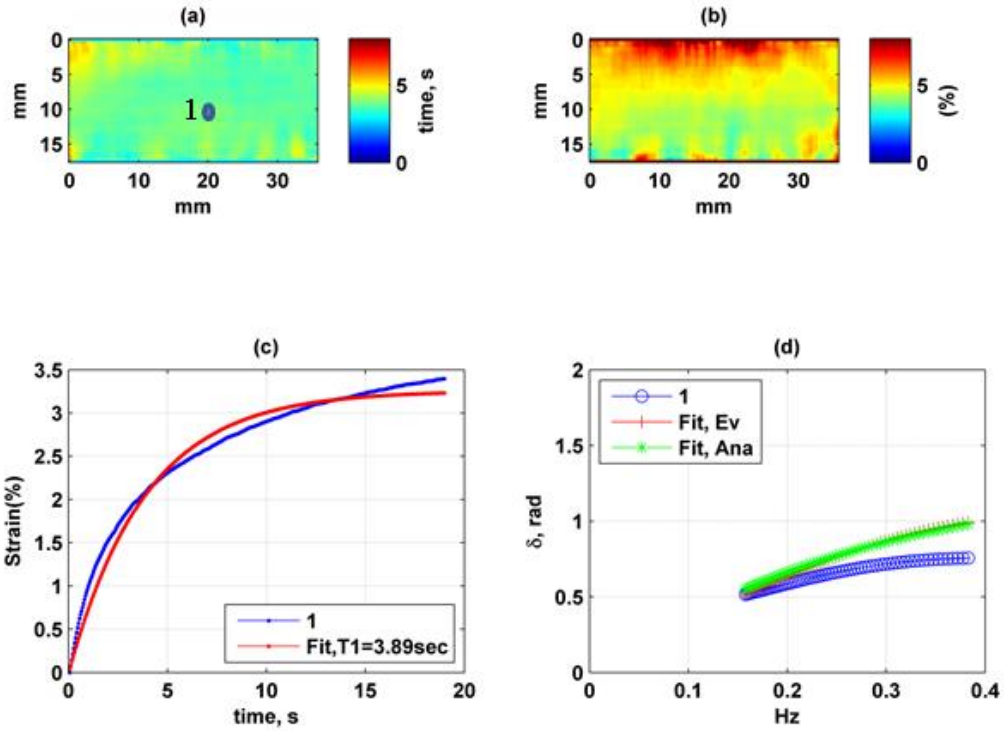

Figure.4.2 Soft uniform phantom. Comparing δ behavior based on the Analytical methods and Evans method. (a) T_1 map (b) Error fit map (c) strain behavior of the point 1 and its Kelvin-Voigt fit with its T_1 value (d) demonstrating the loss angle, δ, behavior resulted from applying Evans method on strain profile of the point 1,blue curve, and applying the Evans method on the fit curve of the strain profile, red curve, and applying the analytical method on fit curve ,green curve.

The same procedure is applied for all the point in phantom to construct the δ map at 0.16 Hz frequency as is observed in Figure.4.3. In this figure in part (a) the δ map is made based on applying the Kelvin-Voigt model or the analytical methods on strain profiles of each point. Part (b) of this figure shows the δ map after applying the Evans methods on strain profile of each point in phantom.

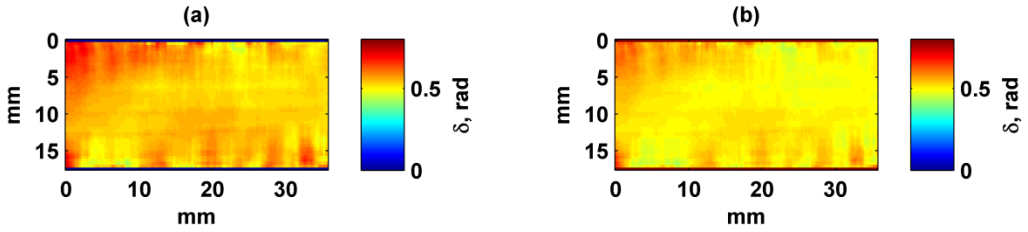

Figure.4.3 Soft uniform phantom .Comparing δ behavior based on the Analytical methods and Evans method. (a) δ map based on applying Kelvin -Voigt methods ,Analytical, on fitted curve of strain profile (b) δ map based on applying Evans methods on strain profile.

We measured the relative error, Eq.(2.8), between the analytical δ map after applying the Kelvin-Voigt model, Figure 4.3 (a), and δ map of strain data after applying Evans' method ,Figure 4.3(b), the error is :3.5 % .

4.3.2 Inclusion phantom:

The same inclusion phantom that we used in the previous Chapter, to test the repeatability of the compression creep device has been applied here. The T_1 value for this phantom has been measured in previous work and so the same data set has been used to measure the δ for this inclusion phantom. A 8N force and ramp of 16 N/s was applied for 20 seconds. Two seconds of initial strain response have been truncated in order to be sure that the force has reached its steady state. Figure 4.4 shows the B-mode image of inclusion

phantom with specified points, and the strain and δ profile related to these points is shown in Figures 4.5(a)-(b).

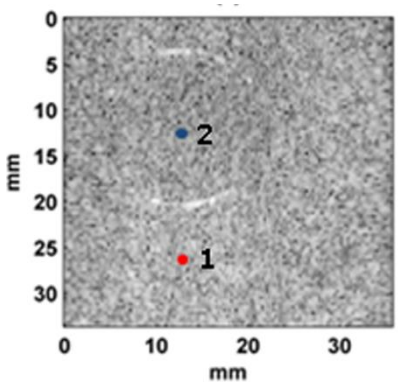

Figure 4.4 Ultrasound B-mode image of inclusion phantom.

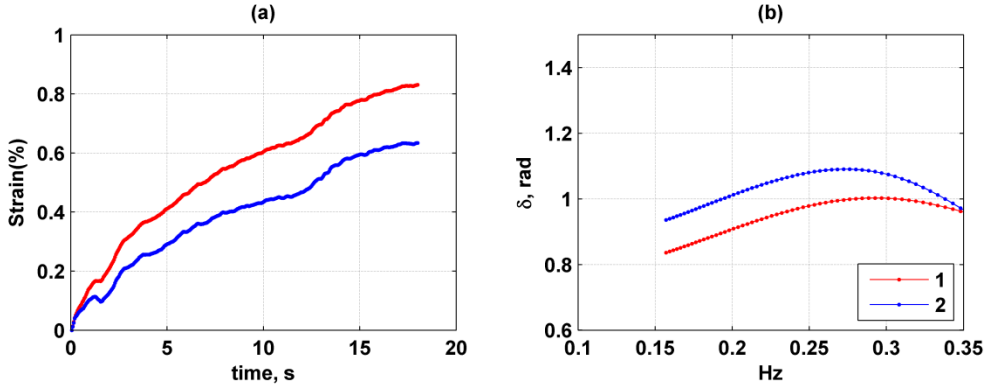

Figure 4.5 (a) Strain profile of points specified in figure 4.3 (a). (b) δ profile of points specified in figure 4.2.

For the inclusion which is stiffer and has lower strain, Figure 3.2(c), and higher T_1 value, Fig.3.3(c), within the frequency range of less than 0.3 Hz, The δ is elevated compared to background which is softer with lower T_1 value.

Figure .4.6 demonstrates the loss angle, δ, maps made at the frequency ranges less than 0.3 Hz.

In this range of frequency in resulting map there is a clear contrast between the inclusion and the background, especially in lower frequencies.

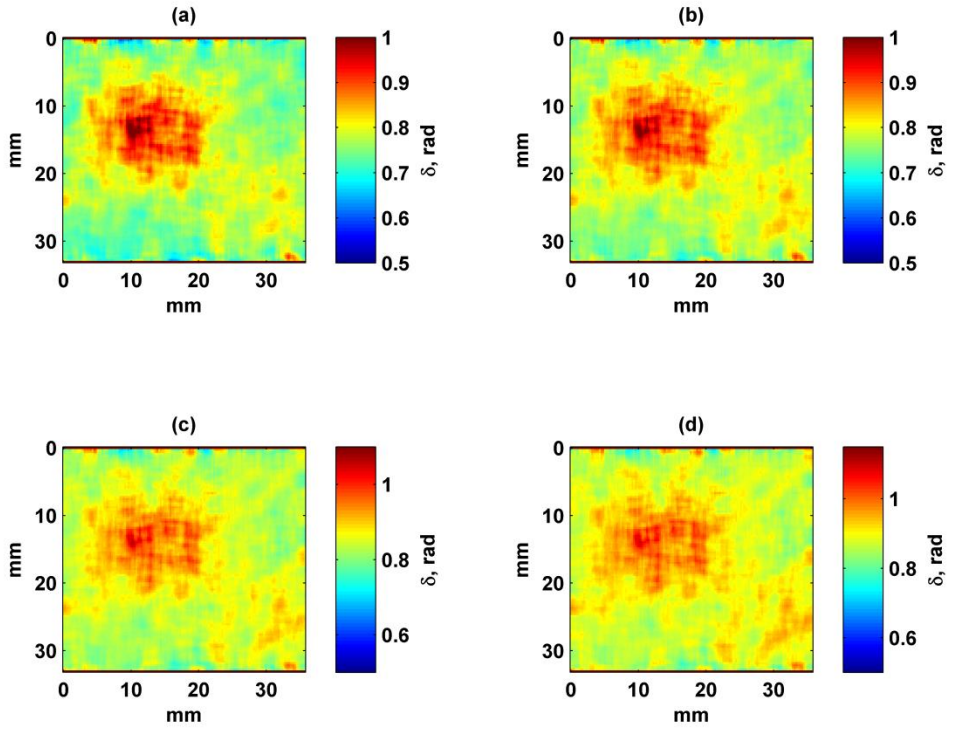

Figure.4.6 δ maps for frequency less than 0.3 Hz for three trials on inclusion phantom. (a) δ map at 0.16 Hz. (b) δ map produced at 0.19 Hz. (c) δ map produced at 0.23 Hz.(d) δ map produced at 0.26 Hz.

4.4 Comparing the loss angle, δ, behavior in sub-Hertz frequency range with retardation time, T_1

Ideally, the retardation time T_1 should be estimated under a constant stress test which is practically impossible due to a sudden jump in stress. In practice this jump is replaced by a ramp function that should be excluded from the creep analysis.

Choosing the initial point is a challenging part of measuring the retardation time, T_1, to evaluate the viscoelastic properties of the medium. To know exactly where the elastic response ends and the viscoelastic part starts can be

difficult to determine [14]. At the beginning of the creep curve response there is a mixture of elastic and viscoelastic responses. These factors can have an influence on the initial part of creep response. Our previous remedy was to truncate the initial part of creep response to eliminate the confusion. The surface force profile resulting from the creep device was a tool, for deciding how much initial time to cut. When the force profile reaches the steady state then definitely the viscoelastic response of the medium is initiated as we explained in chapter 2.

In this part of this Chapter we will show that the sensitivity of the δ to the initial point is much less than retardation time in viscoelastic phantoms. The reason is that sub-Hertz range of frequency of the creep response is associated with the end of the creep response in time domain. The initial part which is mostly related to high frequency components does not have a dominant effect on δ in sub-Hertz frequency range.

We used the same uniform phantoms that were used in Chapter 3. . Figures 3.3(a) and 3.3(b) shows the retardation time maps of these two phantoms. The initial truncation point for this map is after 2 seconds.

Figure 4.7 shows the retardation time map of soft and stiff uniform phantoms with a truncation points of 1 second, shown in Figures 4.7(a) and 4.7 (c), and for truncation time of 3 seconds, illustrated in Figures 4.7 (b) and 4.7(d) respectively.

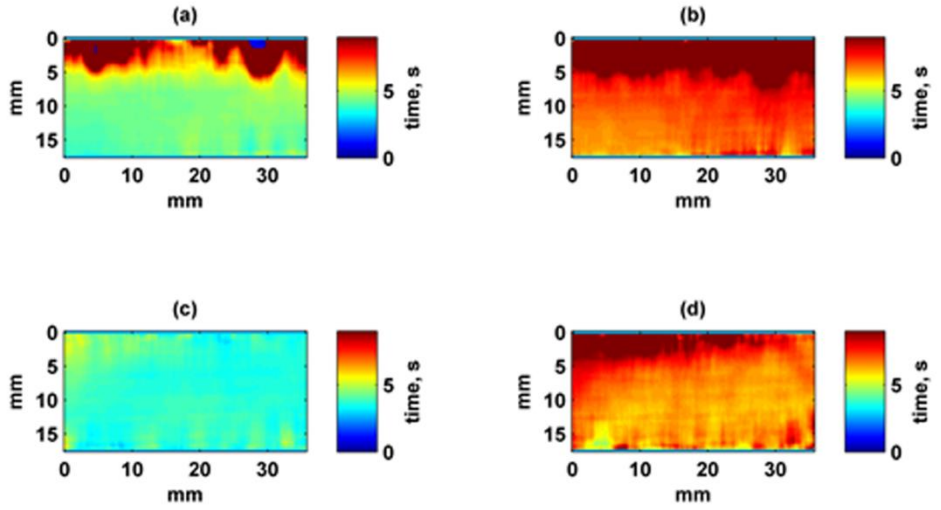

Figure.4.7.Retardation time maps, T_1, for different cutting point in stiff and soft uniform phantoms. (a) T_1 map of stiff uniform phantom with cutting point of 1 second. (b) T_1 map of stiff uniform phantom with cutting point of 3 seconds. (c) T_1 map of soft uniform phantom with cutting point of 1 second. (d) T_1 map of soft uniform phantom with cutting point of 3 seconds. The retardation time map has been elevated in Figure 4.7 (b) and (d) compared with (a) and (c).

To see how the change in the cutting point can affect the fitting error, the fitting error map related to each map in Figure 4.7 is illustrated in Figure 4.8. To make these maps we used the same procedure as explained in Chapter 2, Eq. (2.7).

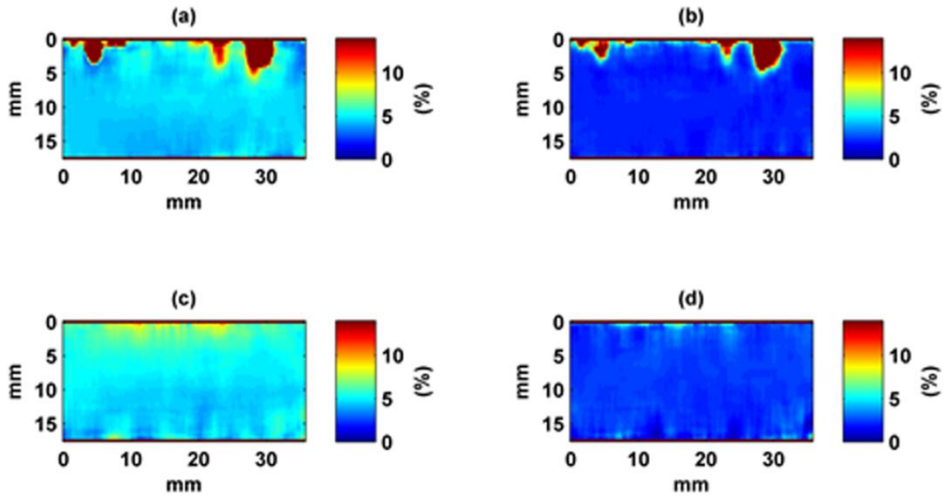

Figure.4.8.Fitting error maps for different cutting point in soft and stiff uniform phantoms. (a) Fitting error map of stiff uniform phantom with cutting point of 1 second. (b) Fitting error map of stiff uniform phantom with cutting point of 3 seconds. (c) Fitting error map of soft uniform phantom with cutting point of 1 second. (d) Fitting error map of soft uniform phantom with cutting point of 3 seconds.

For the next step we created the δ maps, Eqs. (4.8-4.10), based on the same cutting points as in Fig. 4.7. The resulting maps are demonstrated in Figure. 4.9.

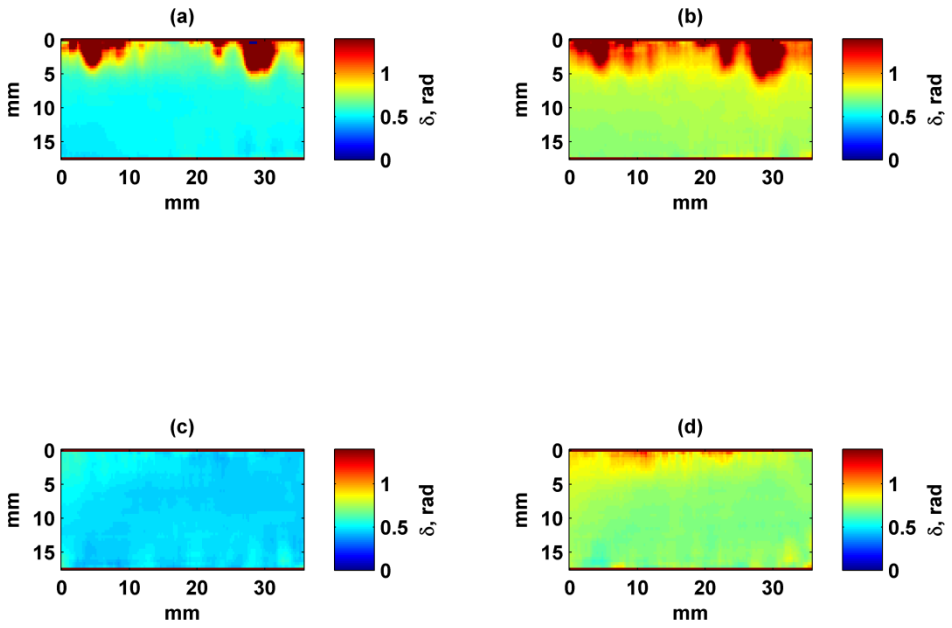

Figure.4.9.δ maps created at 0.17 Hz, for different cutting point in stiff and soft uniform phantoms. (a) δ map of stiff uniform phantom with cutting point of 1 second. (b) δ map of stiff uniform phantom with cutting point of 3 seconds. (c) δ map of soft uniform phantom with cutting point of 1 second. (d) δ map of soft uniform phantom with cutting point of 3 seconds.

The same procedure has been repeated for the inclusion phantom. Figure 4.10 clearly indicates that the retardation time has been increased by changing the initial cutting point. The error fit has been decreased by increasing the cutting point, but overall it is less than 10%.

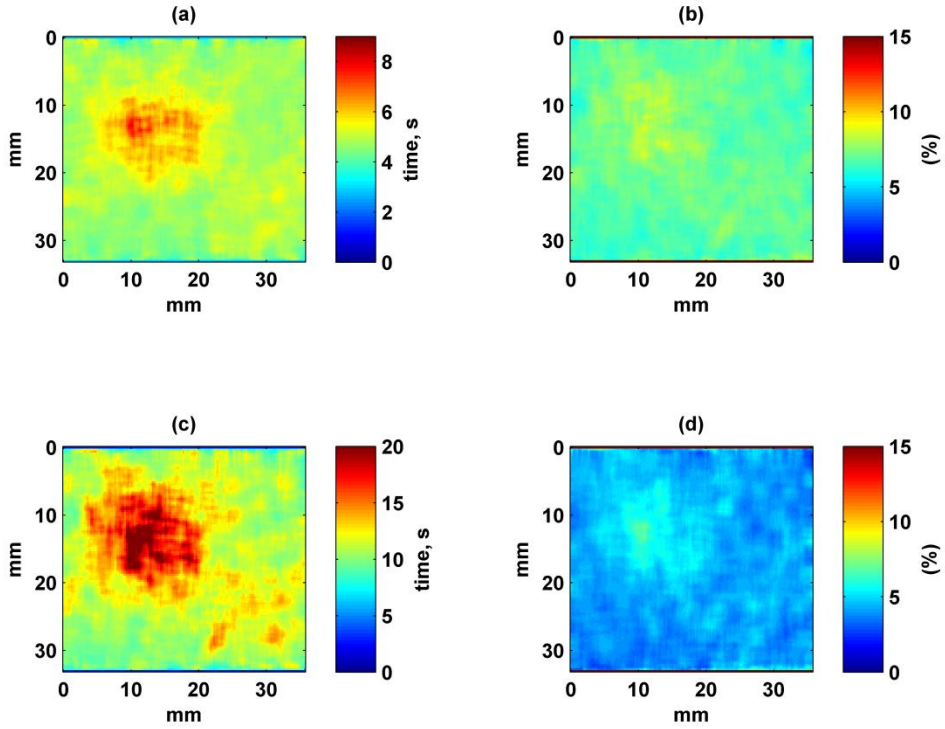

Figure.4.10. Retardation time maps, T_1, and Fitting error map for different cutting point in inclusion phantom.(a) T_1 map of inclusion phantom with cutting point of 1 second. (b) Fitting error map of inclusion phantom with cutting point of 1 second. (c) T_1 map of inclusion phantom with cutting point of 3 seconds. (d) Fitting error map of inclusion phantom with cutting point of 3 seconds.

Simillar to what has been done for uniform phantom, the δ maps with different initial cutting points were constructed. Figure 4.11 shows the resulting δ maps. As is clear in this figure, there is an increase of δ value by increasing the cutting point; however, in the next section, we will show that this increase is much less than the alteration in T_1 maps with the same amount of change in initial cutting points.

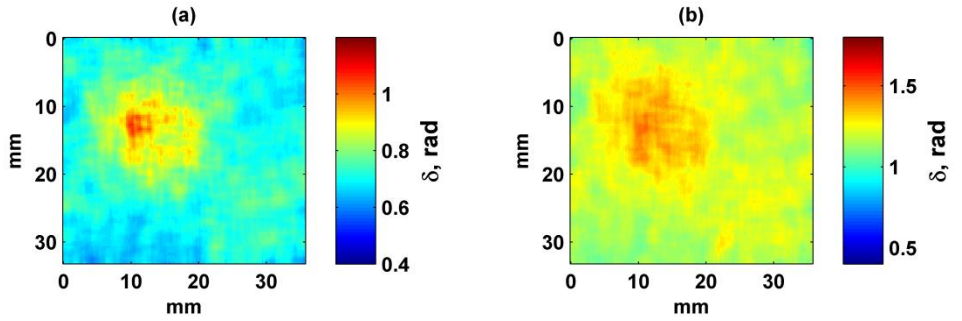

Figure.4.11 δ maps created at 0.17 Hz, for different cutting point in inclusion phantom. (a) δ map of inclusion phantom with cutting point of 1 second. (b) δ map of inclusion phantom with cutting point of 3 seconds.

4.4.1 Quantitative Comparison of δ maps in sub-Hertz frequency range with, T_1 maps at different cutting initial points.

In the previous section we showed the maps of both δ and T_1 based on different cutting points, 1 second and 3 seconds, for soft and stiff uniform phantoms and also for inclusion phantom. In this section we calculate quantitatively the amount of bias for retardation time measurement, T_1, and δ measurement.

In order to define the bias we used the Eq.(4.14).

$$BR = \frac{MH - ML}{ML} \qquad (4.14)$$

where *BR* is the Bias Ratio, *MH* is the mean value of highest elimination frames, in our case it is the mean value of resulted maps with 3 seconds cutting points. and *ML* is the mean value of lowest elimination frames which is the resulting map with 1 second cutting point.

Table 4.1 Bias Ratio, BR, for T_1 and δ measurement in different phantoms.

BR	Soft uniform Phantom	Stiff uniform phantom	Inclusion phantom
T_1	4.29	7.04	9.06
δ	0.16	0.12	0.4

The values in Table 4.2 confirm that the Bias Ratio for δ calculation at sub-Hertz frequency range, 0.17 Hz, has much less variation for all kinds of phantoms comparing to T_1 variations. The sensitivity of δ calculation to initial cutting frame in such frequency range is lower compared to the T_1 value. At this range of frequencies, less than 0.3 Hz, the high frequency ranges that are associated with the initial part of creep response are not involved.

4.5 Discussion:

The main focus of this Chapter is to introduce a method to measure the phase difference between relative storage and loss modulus based on temporal strain profile in frequency domain to observe the contrast in the medium due to its viscoelastic properties in sub-Hertz frequency range. In addition, this method is a model-independent method in which no curve fitting is required. In other words, this new method deals directly with the data, not the fitted curve of the data [32].

As we explained and showed in the previous Chapter the Kelvin-Voigt model is a well-known model to simulate and characterize the creep response in tissue mimicking phantoms, Figure 3.4. This model was applied to validate the frequency methods at low frequency ranges for δ. As the simulation results showed, these two independent methods corroborate well in less than 0.3 Hz frequency range.

It should be noted that when it comes to creep response, the distribution of local stress inside the compressed medium is the main challenging part for these methods. It is impossible to find this distribution based on forward methods [70]. Due to this ambiguity of internal stress distribution in the medium, it is not possible to quantify the Young's modulus based on these methods. Thus all the parameters that can be extracted from strain profiles are relative. This is the reason that in frequency domain, the measured storage and loss modulus are relative. However, when it comes to measuring the phase difference between them, tan (δ) or δ, the effect of the stress distribution is eliminated [20]. Generally this method is applied to elevate the specificity and contrast rather than quantitative measurement [23].

Figure 4.6 illustrates the δ profiles related to the creep responses of the points inside and outside of the inclusion and it is obvious that there is a good contrast between the profiles in frequency ranges less than 0.3 Hz. It has also been shown that the creep response of these two points follows the Kelvin-Voigt model with residue error less than 15 %. Thus for the medium with similar creep response it is possible to evaluate their viscoelastic properties in frequency range less than 0.3 Hz.

The evaluation of the visco-elastic creep response of the medium in the frequency domain based on the phase difference, δ, in sub-Hertz frequency ranges have some other advantages compering to retardation time measurement,T_1, in the time domain.as it was shown it has much lower sensitivity to initial truncating point. In this Chapter we discussed these benefits of the frequency method in three different phantoms. In addition to these benefits, the low computational cost comparing to retardation time methods should not be ignored. The future work is the application of this new method in a group of patients.

4.6 Conclusion:

In this Chapter we described a model-free method for analyzing the viscoelastic strain response in creep test. To validate the new method, we used simulation and compared the analytical results with Kelvin-Voigt model.

To examine the performance of this new method in real situations, we applied it on different mimicking tissue phantoms and described the advantages of this novel frequency based method over the conventional time domain methods.

4.7 Contributions:

- Introducing a new method, δ method, to evaluate the VE creep response in sub-Hertz frequency range, instead of using time domain method like retardation time method, T_1.
- Validation of the new methods based on Kelvin-Voigt model.
- Showing the advantages of δ method over the retardation time methods.

Chapter 5:

Differentiation between benign and malignant tumors by applying sub-Hertz phase difference method, δ.

Introduction

Breast cancer is the fifth most fatal cancer. The diagnosis rate of new cases for invasive breast cancer among US women was estimated at 231,840 in 2015 and 40,290 patients died from this disease and the breast cancer rate is in second position after lung cancer rates among the women [71].

Biopsy is still the most reliable method of diagnosis; however, this procedure is invasive and expensive and can cause pain and discomfort for patients. The need for biopsy can be reduced by increasing the specificity through noninvasive diagnostic imaging.

It is useful to apply indirect methods to explore the intrinsic tissue properties (e.g biochemical, or mechanical) to detect the local alteration in soft tissue especially for breast. The inflammation occurring in the early stage of disease development is accompanied by changes in viscoelastic properties of the tissue. At the microscopic scale, the extra cellular matrix of breast stroma, will experience such changes [71].

As it was explained in previous Chapters, the creep test has the ability to describe the local viscoelastic properties of the medium based on either measuring the retardation times of the creep response in time-domain or measuring the phase difference of relative loss and storage modulus in frequency domain. Based on the former, a patient study was done by Qui *el al.*[14] which shows the ability of the T_1 value to discriminate between benign and malignant tumors which were nonpalpable.

In Chapter 4 we introduced the phase difference, δ, method and its advantages over the retardation time method. Therefore in this Chapter we will show the results of applying the δ method on 31 patients and its ability to discriminate between benign and malignant cases based on contrast values.

The remainder of this Chapter is organized as follows, section one explains a simulation to show the cardiac and breathing motion effect on δ methods. In section two we will briefly explain the methods. In section three the results will be illustrated. The discussion part is in section four and the Chapter will end with a conclusion and contributions in sections five and six respectively.

5.1 Simulation

5.1.2 Heart beat motion effect

When it comes to applying the creep test on a breast patient, there are always two sources of motions that can have a negative influence on recorded data or resultant images: respiration and cardiac motion.

In our patient study, for the initial 10 seconds we asked the patient to stop breathing, which has a great influence on the quality of recorded data. However, heart beat always affects local creep response of breast tissue.

In this part of this Chapter we tried to simulate the heart beat's effect on the creep response. We added a 1 Hz sinusoidal curve to a single exponential curve. Figure 5.1 shows the effect of the heart beat on the δ profile.

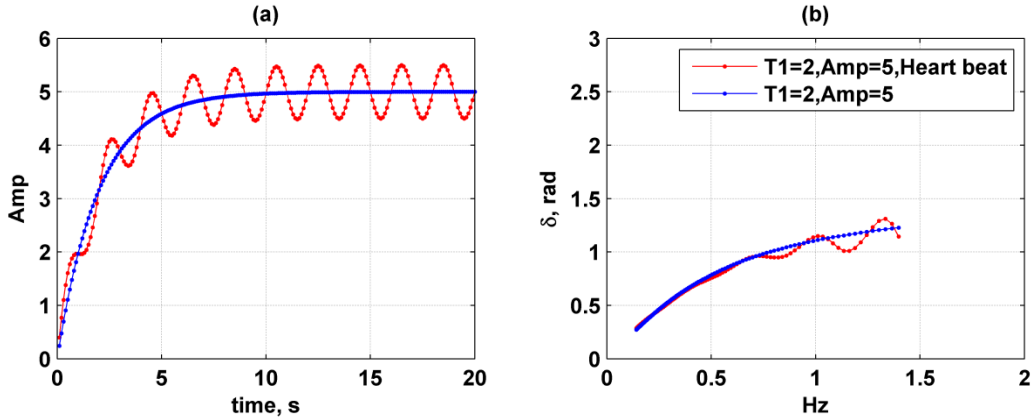

Figure.5.1 Comparing the effect of heart beat on δ in frequency range of less than 2Hz. (a) one exponential input with and without heartbeat. (b) δ profile in frequency range less than 2 Hz.

As observed in Figure 5.1 the motion from the heartbeat does not affect the δ profile significantly in the frequency range less than 0.4 Hz.

5.1.3 Respiratory and heart beat motion effect

In healthy adult the common respiratory rate is between 12-20 breaths per minute in other words the breathing frequency range is between 0.2 Hz to 0.33 Hz [74]. Thus in frequency range less than 0.2 Hz there is no breathing influence.

We used the 0.18 Hz sinusoidal curve to simulate the breathing motion and then it was combined with the heart beat simulated curve, Figure 5.1. The modulated signal is demonstrated in Figure 5.2(a). As it is evident in Figure 5.2(b) in frequency range less than 0.18 Hz the modulated creep response and unmodulated one have the same responses and cover each other well.

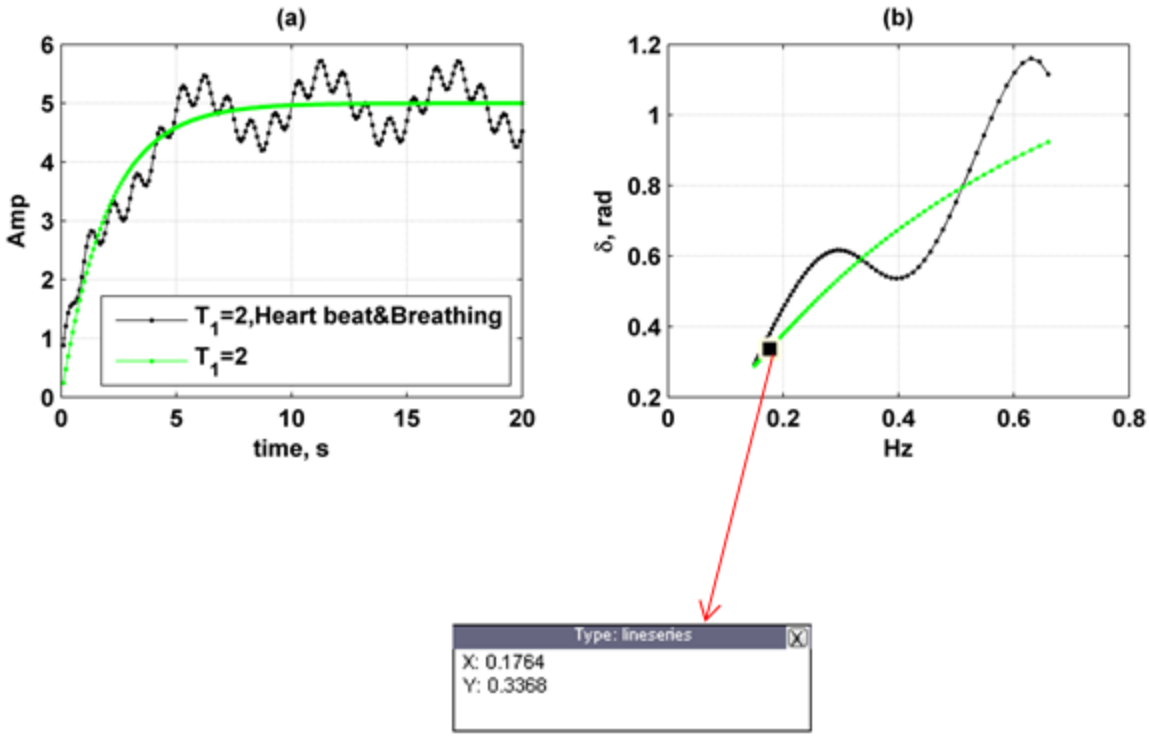

Figure.5.2 Comparing the effect of heart beat,1 Hz, and breathing, 0.18 Hz, together on δ in frequency range of less than 0.8 Hz. (a) one exponential input with and without heartbeat and breathing. (b) δ profile in frequency range less than 0.8 Hz.

This is another benefit of using δ profile in sub-Hertz frequency range to analyze the creep response in *in vivo* breast study. This simulation shows that in the worst case scenario, if the patient is not able to hold her breath during the creep test it is still possible to measure the loss modulus at low frequency range less than 0.2 Hz.

5.2 Material and Methods

For this study, a 2 N force with ramp of 8 N/s was applied by the automated creep device, explained in Chapter 2, and the data was recorded for 30 seconds; We asked the patient to hold her breath for 10 seconds, and the results were based on the processing of that initial 10 seconds of data which were without breathing.

To ensure that the force has reached steady state, more than a quarter of second of initial strain data was excluded. In this study based on this creep response we applied Evans' method [32] and extracted the δ behavior in frequency range less than 0.3 Hz. The pulse repetition frequency, or PRF, was 200 Hz for these patient studies. To construct the δ map as explained in Chapter 4, Eqs. (4.8)-(4.10) have been employed.

5.3 Patient selections

The data were acquired from 31 female patients through the breast clinic at Mayo Clinic. The patients were screened by mammography before our study. After our study each patient went for the core needle biopsy procedure.

The protocol was approved by the Institutional Review Board at Mayo Clinic. Among these 31 patients, 16 cases were diagnosed with a benign lesion and 15 with a malignant one.

Figure, 5.3 shows the B-mode image and the registered δ map with the B-mode image. This data is from the same malignant patient that was shown in Figure 3.6 in Chapter 3.

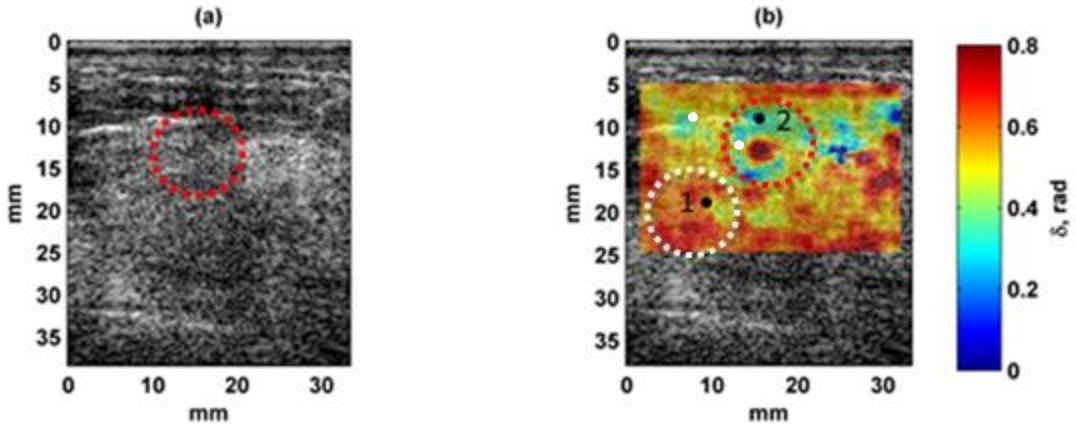

Figure.5.3 (a) B-mode image of the malignant patient. The red circle shows the location of the malignant tumor. (b) Registered δ map created at frequency 0.14 Hz for benign patient.

The malignant lesion shows a lower δ value compared to the background. Figure 5.4 depicts in more detail the behavior of two specified points, 1 and 2, in Figure 5.3 (b). In Figure 5.4 (a) the strain of these points is shown and Figure 5.4 (b) illustrates their behavior in the frequency range of less than 0.35 Hz. In Figure, 5.4 (a), the background strain is higher than the tumor strain which means the tumor is stiffer than the background due to tumor's lower strain.

In Figure 5.4(b) the δ profile is elevated for the background compared to the lesion in the frequency range less than 0.3 Hz. Comparing Figures 5.3(b) and 3.6(b) reveals that the T_1 value is decreased for tumor areas compared to the background and the same pattern occurred in Figure 5.3(b) for δ maps.

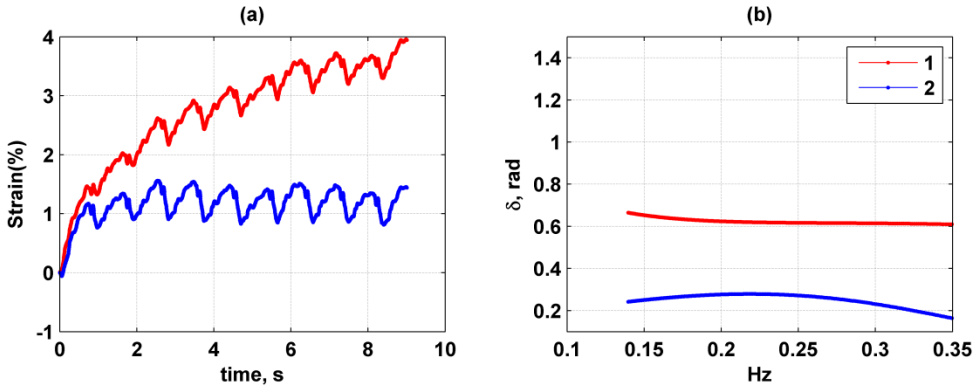

Figure.5.4 (a) Strain profiles of two specified points in figure 5.3 (b). (b) δ profiles of corresponding points.

The same process is repeated for benign cases. The same data from Chapter 3, Figure 3.5, is used here to measure the δ value for each point and create maps at different sub-frequency ranges. Figure 5.5 demonstrates the B-mode and the registered δ map for a benign case.

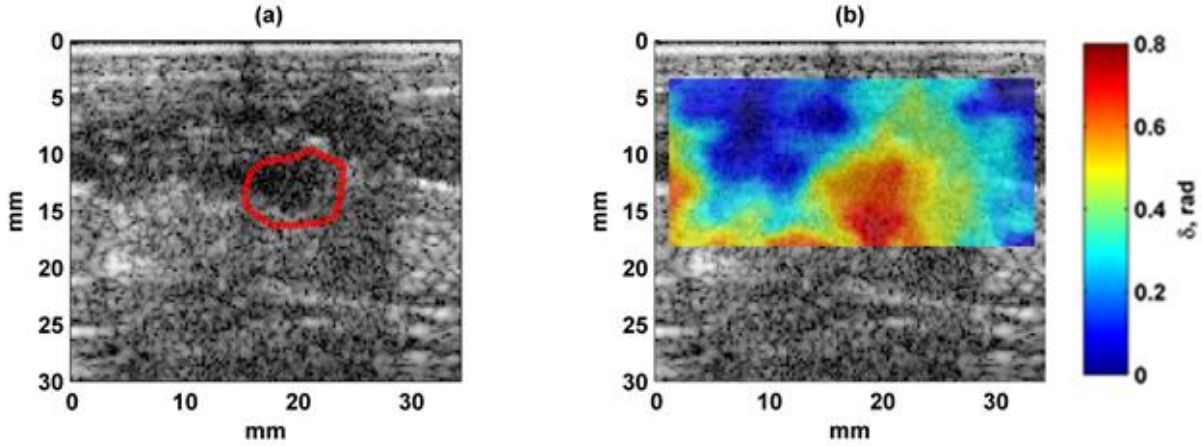

Figure5.5 B-mode image of the benign patient. The red circle shows the location of the malignant tumor. (a) B-mode image (b) δ map created at frequency 0.14 Hz.

In Figure 5.5 the δ map follows the same pattern as we discussed previously. In benign cases, T_1 value for lesion is greater than back ground, Figure 3.5(b). In δ maps in low frequency ranges the δ value is higher for a benign tumor compared to back ground tissue as it is obvious in Figure 5.5(b).

5.4 Contrast measurement:

Contrast plays an essential diagnostic role in differentiating between malignant and benign tumors [14].Contrast is calculated using Eq. (5.1),

$$C = \frac{X_{lesion} - X_{background}}{\left(X_{lesion} + X_{background}\right)/2} = \frac{Difference}{Average} \qquad (5.1)$$

In this equation X_{lesion} is the mean value of loss angle in inclusion part and $X_{background}$ represents the loss angle value of the background in the phantom or tissue. Figure 5.6(a) shows the loss angle map of the another malignant case. In part (b) of this figure we show the quality mask map. in next section it will be explained in more details. Part (c) and (d) of this figure respresnt the applied mask to measure mean value for inclusion and background part respectively. The non zero parts in these parts are considered for measuring the contrast value.

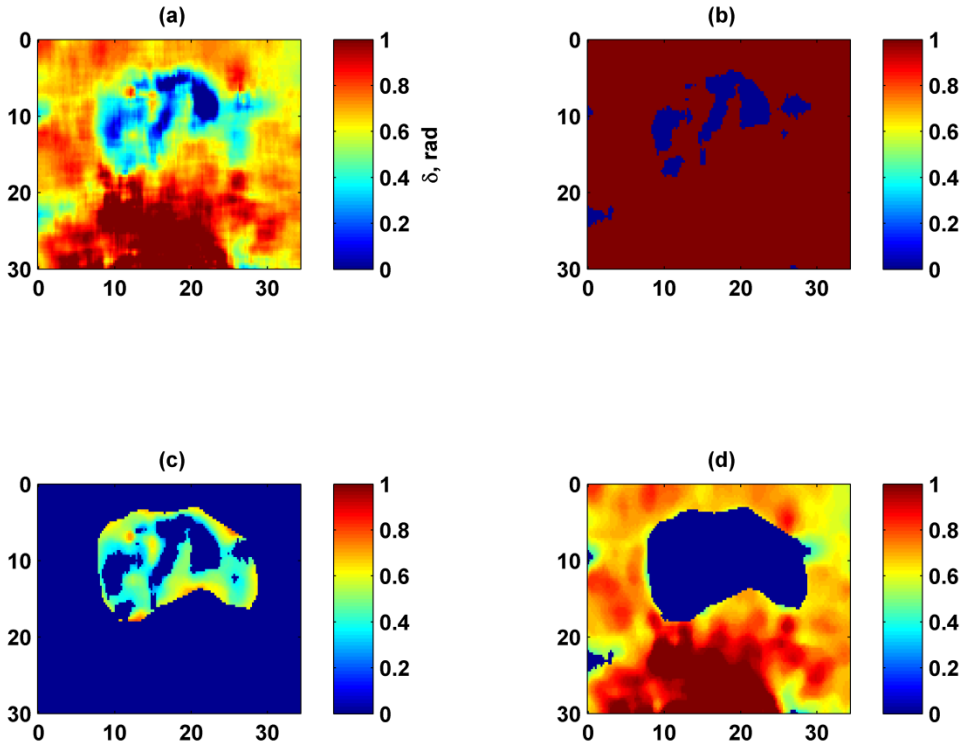

Figure.5.6. Malignant case (a) loss angle map (b) Quality mask (c) lesion mask for measuring loss angle of inclusion part (d) back ground mask for measuring the loss angle of background part.

so based on these resulted map the measured contrast value of loss angle is -0.5.

5.4.1 Quality mask measurement

We defined a parameter as quality mask measurement in order to evaluate the strain behaviour of each point in the medium while applying compression. sometimes due to mobility of inclusion or fluidic nature of some parts of the medium the strain behavior of those parts do not follow the same trend as the normal part do. In Figure 5.7 we have simulated those unsual strain behavior. for example , the blue color strain profile represents the strain behavior of inclusion mobility of a point around the inclusion while applying the compression. as is obvious the slope of the

strain profile is negative at the end of the profile. Another situation could happen if some part of the medium is fluidic, green color.

To investigate what will happen on loss angle profile in mis-behaved situations as mentioned before, we did a simulation as illustrated in Fig.5.6. in this figure when some mis-behaved conditions happened the loss angle at low frequency will be negative.

The quality mask, figure 5.7(b), is constructed based on the evaluation of the positivity of the loss angle sign, thus the well behaved ones are considered as value one, and the mis-behaved ones are supposed to be zero.

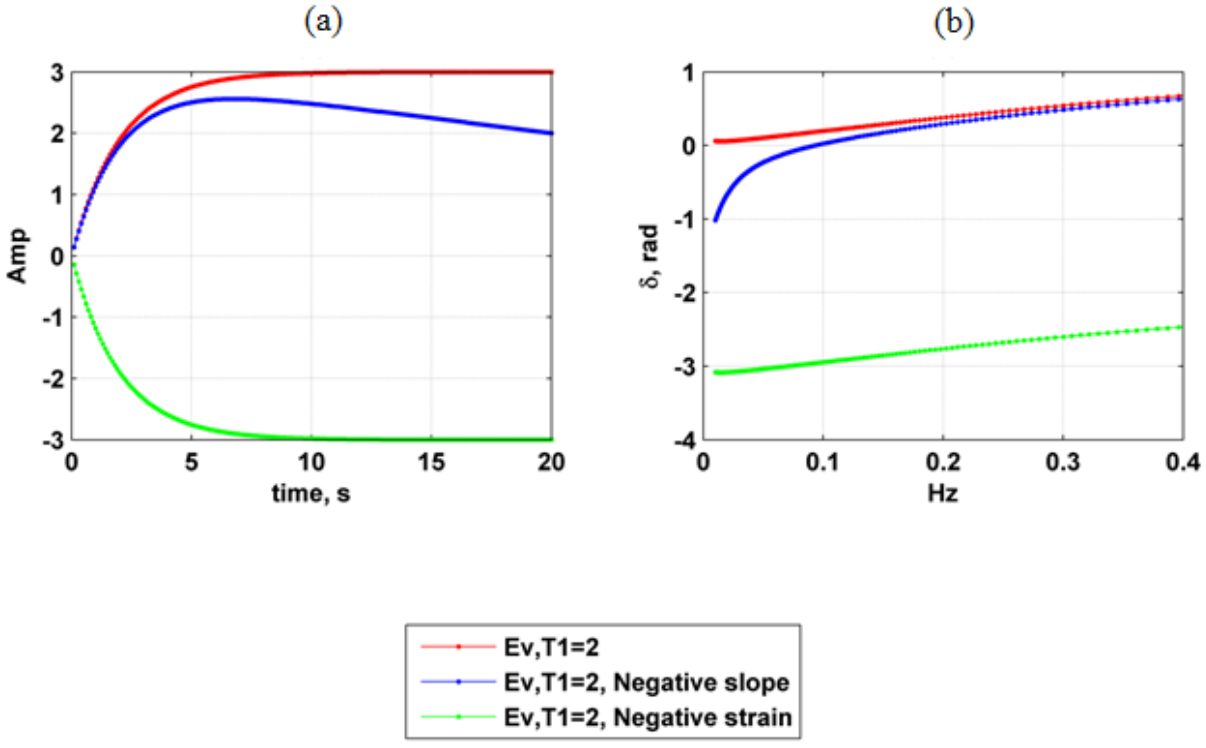

Figure.5.7. simulation results. (a) strain profiles, (b) Loss angle profiles

It seems that for malignant case illustrated in figure 5.6 there are some points in the lesion do not have a well behaved strain behavior, zero value

5.6(c) however almost all the points in background have well behaved behavior.

According to Eq. (5.1) the measured contrast of the δ map for the benign case, Figure 5.1(b), is 1.8 and for malignant case, Figure 5.3(b), is -0.4.The contrast value is measured for 31 breast patients including, 16 benign cases and 15 malignant cases.

BI-RADS or Breast Imaging Reporting and Data System (BI-RADS) lexicon for ultrasonography (US) which allocates a grade to a lesion based on its situation. This grade range is between1 to 5. Among these range for grade less than 2 means there is no risk involved. If the grade is 2 the lesion is benign; for lesion with grade of 3 means the lesion is benign but a short period of follow up is needed. When it comes to grade 4 the biopsy is necessary but this grade can be divided in three sub categories 4A, low suspicion for malignancy, 4B, intermediate suspicion of malignancy, and 4C, moderate suspicion of malignancy. And grade 5 is highly suggestive of malignancy which needs biopsy [73]. Among our patients group the majority of them are BIRADS 4 but there are some cases of BIRADS 3 and 5 too.

Figure 5.8 shows the δ contrast results in 31 breast patients. As is obvious in this figure these two different types of masses are completely differentiated.

For benign cases the δ contrast is positive while for malignant ones it is negative.

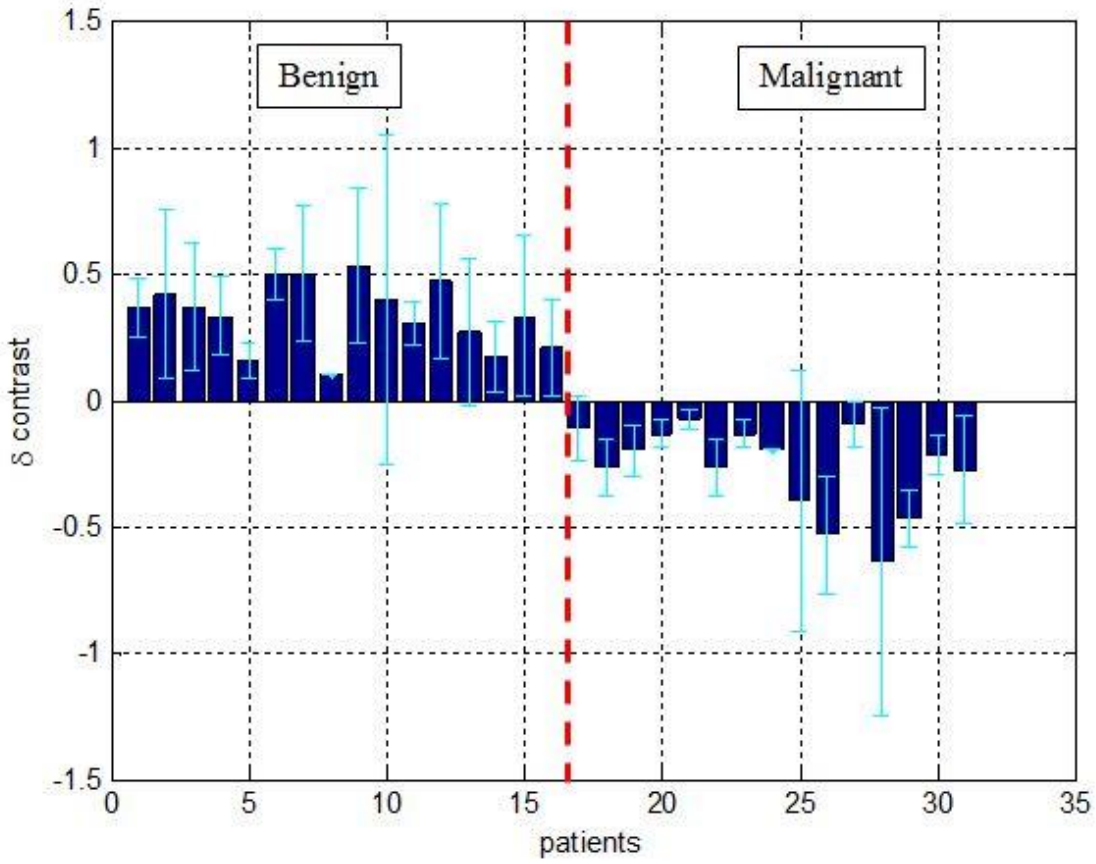

Figure.5.8 bar graph for 31 patients. The first 16 patients with positive δ contrast are benign and the 15 patients with negative δ contrast are malignant.

5.5 Comparison of the creep patient results with Shear wave elastography methods.

Denis *et al*.[8] reported the use of Comb-push Ultrasound Shear wave Elastography of breast masses in detail and its patients study results. In this paper, a threshold has been suggested to categorize the tumors in benign and malignant group. This threshold was determined based on measuring the shear wave speed and the resultant Young's modulus value in benign and malignant breast tumor. This study suggests that for benign tumors their young's modulus is less than 68 kPa while the measured Young's modulus for malignant tumors are more than this value.

In parallel with the patient creep study in which the results were reported in the previous section, shear wave elastography was alzo applied on the same patients. Comparison between the high frequency range, shear wave elastography methods, and the low frequency range, δ methods, reveals that the specificity of the latter is higher than the former. In other word, there are a few cases that δ method has predicted the tumor type accurately while shear wave elastography results failed.

Figure .5.9 shows a shear wave map result in a patient with a tumor. The measured Young's modulus for this case is 106.74 ±9.61 kPa.

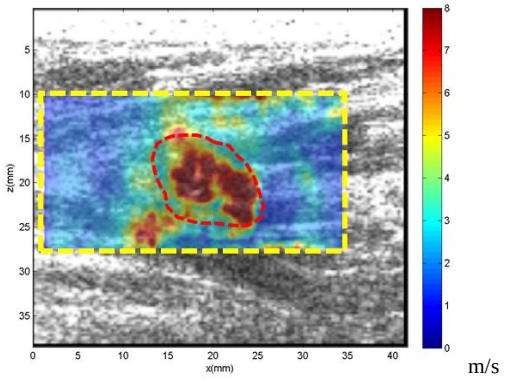

Figure.5.9 Shear wave speed map registered on B-mode image of breast tumor.

Based on the shear wave speed map and its resultant Young's modulus values, this case should be a malignant case,[8] but according to biopsy results this case is a benign tumor. Figure 5.10 illustrates the δ map result of the same breast patient. The measured contrast for this case is 0.07, Eq.5.1, which is positive and indicates that this is a benign tumor.

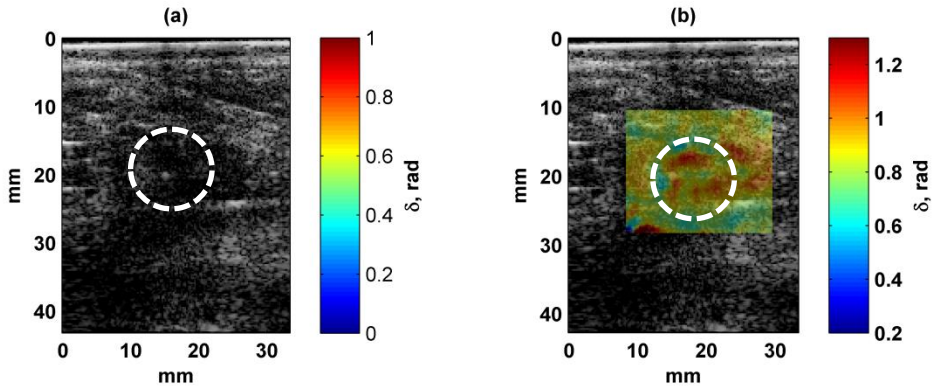

Figure.5.10 Benign case (a) B-mode image. (b) Registered δ map on the same B-mode image.

5.6 Discussion

The preliminary clinical data that was shown in this Chapter proves that the viscoelastic properties of the breast lesions are helpful to distinguish between malignant and benign tumors. The δ method that was described in the previous Chapter showed a significant difference between these two types of lesion. Moreover, for malignant lesions the δ contrast was negative, while it was positive for benign ones in all patient studies.

Generally in benign tumors, the proteoglycan content increases which can cause the elevation of normal collagen density. When the density of the normal collagen or ECM increases, both the cross-linking among the collagen fibers and consequently the viscosity of interstitial fluid will increase. This phenomenon will cause resistance to creep and elongate the T_1 values, Eq.4.3, [14] .This resistance to the creep can have the same effect on δ behavior.

Elevation of collagen density can occur in malignant tumors too, however these collagen fibers are not the same as the normal collagen or ECM stroma. Also the reduction of proteoglycan content is conspicuous in

malignant lesions compared to benign ones. These factors will lead to less frictional forces resisting creep. Therefore, T_1 value for malignant lesion is lower compared to the T_1 value for background or normal breast stroma for malignant cases [14]. In other words, in contrast to benign lesions which are more in solid form, the malignant lesions are more fluidic [14]. Thus δ value for a malignant tumor is less than its background, the same occurs for its T_1 value.

One of the main advantages of this patient study is the application of the Automated Compression Device, Chapter 2. It is shown that a small movement due to hand-held transducer during force application can elevate the de-correlation errors in strain images [74].In addition to transducer movement, there are other sources of patient movements like respiratory and cardiac which can cause error in viscoelastic imaging [14]. In this study all of these sources of error have been considered and efforts were made to decrease their influence. For respiratory movement, patients were asked to stop breathing for 10 seconds. For cardiac motion as it was shown in this Chapter, in sub-Hertz frequency range, less than 0.3 Hz, of δ profile the heartbeat motion has no impact.

Another unique characteristics of this study was its high frame rate data acquisition, PRF=200 Hz, which can capture the creep response especially at the beginning of this response which happens very fast. Due to this characteristic, during all of these data acquisitions of patients de-correlation never happened.

As it is shown in simulation and phantom study in previous Chapter T_1 and δ values are directly related and the *in- vivo* results in this Chapter also confirm that for higher retardation time the δ is increased, and the δ is decreased for lower retardation time.

Another point that should be noted is that the tumors can be highly heterogeneous in *in vivo* studies. Sometimes part of this tumor can be very stiff but another part of it may include fluid which affects the resultant non-uniform δ map. Also the mobility of some tumors while applying pressure is another problem that should be considered and requires cautions while recording the data.

Choosing the region-of-interest for measuring the δ contrast is to some extent subjective but it is clear in all the resulting δ maps for benign cases the δ value for the lesion part is higher than the background, which means the contrast for such maps is positive, but when it comes to malignant lesions the δ value for the lesion part is lower than its background therefore the contrast value is negative. Thus the sign of the δ contrast is more important than its value.

In all *in vivo* contrast calculation cases, we tried to find the area of the background tissue which shows a consistent homogenous normal glandular/ fatty breast tissue in B-mode images.

The great advantage of the δ method is its ability to distinguish between benign and malignant tumors. As figure 5.8 shows the δ method was able to detect a range of different malignant cases with different BIRADS value. This figure confirms that this method has the ability to detect the malignant tumor in early stages like, BIRADS 3, 4. We hope this characteristic of δ method will help the physician make a more accurate diagnosis for early breast cancer patients. Among all the patient study that were performed with both the shear wave elastography method and δ method, there were some cases that their results from shear wave elastography drew opposite compared with δ methods. One case has been discussed in section 5.8. Because the number of patients is not enough there for it is too soon to have

a conclusion about the specificity of two methods. However, we plan to investigate and compare the specificity of these two methods in the future.

Future efforts will also focus on applying this novel method on a larger group of patients and exploring the ability of δ method to differentiate among various stages of malignancy.

5.7 Conclusion

In this Chapter the phase difference, δ method, was applied to 31 patients. The resultant delta maps and its contrast were able to distinguish between benign and malignant lesions. One of the unique characteristics of this study was the application of the automated creep device on each patient. High frame rate data acquisition was another important aspect of this study.

When it comes to processing part of the data, it was shown that δ method is less sensitive to noise and cardiac motion.

5.8 Contribution:

- Applying the δ method on 31 patients and showing its capability in differentiating between malignant and benign tumors.

Concluding Chapter and future work:

In this PhD thesis, we tried to solve two main problems that were associated with creep test application for *in-vivo* tests. The first problem was the hand-held application of the force to stimulate the creep response in the tissue and the second problem was the fitting method that was used to evaluate the viscoelastic creep response of the tissue.

In this thesis work, we first designed and validated a fully automatic compression device with the ability to maintain the preset force level constant for a predetermined period of time typically 10-100 seconds with the ability to manage the ramp speed of the force. As the phantom study showed the design of the device helps to elevate both the accuracy and repeatability of the creep test.

For the second problem we applied a new method called loss angle which directly dealt with local creep response data. This method was first validated by simulation and then on a uniform tissue mimicking phantom.

Because the local creep response deals with a viscoelastic properties of the breast tissue we expect that this method has higher specificity to differentiate between malignant and benign tumors compared to shear wave elastography methods. Thus the future goal is to apply this method to a large group of patients comparing the methods based on the specificity and ultimately replacing biopsy procedure with this non-invasive method.

Bibliography:

[1] Hippocrates, On the Surgery, 400 BC

[2] Breast Cancer Facts & Figures 2015-2016. - American Cancer Society

[3] M. Tanter, J. Bercoff, A. Athanasiou, T. Deffieux, J. L. Gennisson, G. Montaldo, M. Muller, A.Tardivon, and M. Fink, "Quantitative assessment of breast lesion viscoelasticity: Initial clinical results using supersonic shear imaging," *Ultrasound in Medicine and Biology, vol.34, no.9, pp.1373-1386, Sep, 2008.*

[4] D. Cosgrove, F. Piscaglia, J. Bamber, J. Bojunga, J. Correas, O. Gilja, A. Klauser, I. Sporea, F. Calliada, and V. Cantisani, "EFSUMB guidelines and recommendations on the clinical use of ultrasound elastography. Part 2: Clinical applications," *Ultraschall Med,* vol. 34, pp. 238-253, 2013.

[5] A. Sarvazyan, T. J. Hall, M. W. Urban, M. Fatemi, S. R. Aglyamov, and B. Garra, "Elasticity imaging - an emerging branch of medical imaging. An overview.," *Current Medical Imaging Reviews, vol. 7, no. 4, pp. 255-282, 2011.*

[6] D. Carneiro-Pla, "Ultrasound elastography in the evaluation of thyroid nodules for thyroid cancer," *Current Opinion in Oncology, vol. 25, no. 1, pp. 1-5, 2013*

[7] D. W. Good, G. D. Stewart, S. Hammer, P. Scanlan, W. Shu, S. Phipps, R. Reuben, and A.S.McNeill, "Elasticity as a biomarker for prostate cancer: a systematic review," *BJU International, pp. n/a-n/a, 2013.*

[8] M. Denis, M. Mehrmohammadi, P. Song, D. D. Meixner, R. T. Fazzio, S. Pruthi, D. H. Whaley, S. Chen, M. Fatemi, and A. Alizad, "Comb-Push Ultrasound Shear Elastography of Breast Masses: Initial Results Show Promise," 2015.

[9] S. L. Friedman, "Liver fibrosis -- from bench to bedside," *Journal of Hepatology, vol. 38 Suppl 1, pp.S38-53, 2003.*

[10] N. H. Afdhal, and D. Nunes, "Evaluation of liver fibrosis: a concise review," *The American journal of gastroenterology, vol. 99, no. 6, pp. 1160-74, Jun, 2004.*

[11] J. Ophir, I. Cespedes, H. Ponnekanti, Y. Yazdi, and X. Li, "Elastography: a quantitative method for imaging the elasticity of biological tissues," *Ultrasonic Imaging, vol. 13, no. 2,pp.111-34, Apr,1991.*

[12] Fung Y. Biomechanics: mechanical properties of living tissues. Springer-Verlag; 1993

[13] M. Sridhar and M. F. Insana, "Ultrasonic measurements of breast viscoelasticity," *Medical physics,* vol. 34, pp.4757-4767, 2007.

[14] Y. Qiu, M. Sridhar, J. K. Tsou, K. K. Lindfors, and M. F. Insana, "Ultrasonic viscoelasticity imaging of nonpalpable breast tumors: preliminary results," *Academic radiology,* vol. 15, pp.1526-1533, 2008.

[15] T. J. Hall, Y. Zhu, and C. S. Spalding, "*In vivo* real-time freehand palpation imaging,"*Ultrasound in Medicine & Biology, vol. 29, no. 3, pp. 427-435, 2003.*

[16] C. Coussot, S. Kalyanam, R. Yapp, and M. F. Insana, "Fractional derivative models for ultrasonic characterization of polymer and breast tissue viscoelasticity, " *Ultrasonics, Ferroelectrics, and Frequency Control, IEEE Transactions on,* vol. 56, pp. 715-726, 2009

[17] B. Elenbaas and R. Weinberg, "Heterotypic signaling between epithelial tumor cells and fibroblasts in carcinoma formation, " *Exp.Cell Res., vol. 264, pp.169–184, 2001.*

[18] D. E. Discher, P. Janmey, and Y.-L. Wang, "Tissue cells feel and respond to the stiffness of their substrate," *Science,* vol. 310, pp.1139–1143, 2005.

[19] S. Suresh, "Biomechanics and biophysics of cancer cells," *Acta Biomater.*,vol. 3, pp. 413– 438, 2007.

[20] C. Amador, M. W. Urban, S. Chen, and J. F. Greenleaf, "Loss tangent and complex modulus estimated by acoustic radiation force creep and shear wave dispersion," *Physics in medicine and biology,* vol. 57, p. 1263, 2012.

[21] F. W. Mauldin Jr, M. Haider, E. G. Loboa, R. H. Behler, L. E. Euliss, T. W. Pfeiler, and C.M.Gallippi, "Monitored steady-state excitation and recovery (MSSR) radiation force imaging using viscoelastic models," *Ultrasonics, Ferroelectrics, and Frequency Control, IEEE Transactions on,* vol. 55, pp. 1597-1610, 2008.

[22] M. R. Selzo and C. M. Gallippi, "Viscoelastic response (VisR) imaging for assessment of viscoelasticity in voigt materials," *Ultrasonics, Ferroelectrics, and Frequency Control,IEEE Transactions on,* vol. 60, pp. 2488-2500, 2013.

[23] M. Sridhar, J. Liu, and M. Insana, "Viscoelasticity imaging using ultrasound: parameters and error analysis," *Physics in medicine and biology,* vol. 52, p. 2425, 2007.

[24] M. Fortin, M. D. Buschmann, M. J. Bertrand, F. S. Foster, and J. Ophir, "Cross-correlation of ultrasound A-lines to obtain dynamic displacement profiles within poroelastic materials undergoing stress relaxation," in *Medical Imaging 2000*,

[25] T. J. Hall, M. Bilgen, M. F. Insana, and T. A. Krouskop, "Phantom materials for elastography," vol 44, pp. 1355-1365, 1997.

[26] C. Pellot–Barakat, F. Frouin, M. F. Insana, and A. Herment, "Ultrasound elastography based on multi-scale estimations of displacement regularized fields," *IEEE Trans. Med.Imag.*,vol. 23, pp.153–163, 2004.

[27] F. Viola and W. F. Walker, "A spline-based algorithm for continuous time-delay estimation using sampled data," *IEEE Trans.Ultrason. Ferroelectr. Freq. Control*, vol. 52, pp. 80–93, 2005.

[28] G. F. Pinton and G. E. Trahey, "Continuous delay estimation with polynomial splines," *IEEE Trans. Ultrason. Ferroelectr. Freq. Control*,vol. 53, pp. 2026–2035, 2006.

[29] J. R. Doherty, G. E. Trahey, K. R. Nightingale, and M. L. Palmeri, "Acoustic radiation force elasticity imaging in diagnostic ultrasound," *IEEE Trans. Ultrason., Ferroelectr., Freq.Control*, vol. 60, no. 4, pp. 685–701, Apr. 2013.

[30] T. Loupas, J. T. Powers, and R. W. Gill, "An Axial Velocity Estimator for Ultrasound Blood-Flow Imaging, Based on a Full Evaluation of the Doppler Equation by Means of a 2-Dimensional Autocorrelation Approach," *IEEE Transactions on Ultrasonics Ferroelectrics and Frequency Control*, vol. 42, no. 4, pp. 672-688, Jul, 1995.

[31] H. Du, J. Liu, C. Pellot-Barakat, and M. F. Insana, "Optimizing multicompressionapproaches to elasticity imaging,"*Ultrasonics, Ferroelectrics and Frequency Control, IEEE Transactions on*, vol. 53, pp. 90-99, 2006.

[32] R. Evans, M. Tassieri, D. Auhl, and T. A. Waigh, "Direct conversion of rheological compliance measurements into storage and loss moduli," *Physical Review E*, vol.80, p.012501, 2009.

[33] Huwart, F. Peeters, R. Sinkus, L. Annet, N. Salameh, L. C. ter Beek, Y. Horsmans,and B. E. Van Beers, "Liver fibrosis: non-invasive assessment with MR elastography," *NMR Biomed*, vol. 19, pp. 173-9, 2006.

[34] M. F. Insana, C. Pellot-Barakat, M. Sridhar, and K. K. Lindfors, "Viscoelastic imaging of breast tumor microenvironment with ultrasound,",*journal of mammary*

gland biology and neoplasia , vol. 9, pp. 393- 404, 2004.

[35] G. A. Losa and M. Alini, "Sulfated proteoglycans in the extracellular matrix of human breast tissues with infiltrating carcinoma," *International journal of cancer,* vol. 54,pp. 552-557, 1993.*Biomechanical engineering* vol. 131, p. 081005, 2009.

[36] W. N. Findley and F. A. Davis, *Creep and relaxation of nonlinear viscoelastic materials*: Courier Dover Publications, 2013.

[37] D. J. Plazek, "Magnetic bearing torsional creep apparatus," *Journal of Polymer Science Part A-2: Polymer Physics,* vol. 6, pp. 621-638, 1968.

[38] M. Sridhar, J. Liu, and M. F. Insana, "Elasticity imaging of polymeric media," *Journal Of biomechanical engineering,* vol. 129, pp. 259-272, 2007.

[39] D. Chan, C. Neu, and M. Hull, "In situ deformation of cartilage in cyclically loaded tibiofemoral joints by displacement-encoded MRI," *Osteoarthritis and Cartilage,* vol.17, pp. 1461-1468, 2009.

[40] S. Campana, E. Charpail, J. De Guise, L. Rillardon, W. Skalli, and D. Mitton, "Relationships between viscoelastic properties of lumbar intervertebral disc and degeneration grade assessed by MRI," *Journal of the mechanical behavior of biomedical materials,* vol. 4, pp. 593-599, 2011.

[41] J. C. Bamber and N. L. Bush, "Freehand elasticity imaging using speckle decorrelation rate," in *Acoustical imaging*: Springer, 1996, pp. 285-292.

[42] T. Varghese, J. Zagzebski, G. Frank, and E. Madsen, "Elastographic imaging using a Handheld compressor," *Ultrasonic imaging* vol. 24, pp. 25-35, 2002.

[43] K. M. Hiltawsky, M. Krüger, C. Starke, L. Heuser, H. Ermert, and A. Jensen, "Freehand Ultrasound elastography of breast lesions: clinical results," in *Acoustical imaging, ed: Springer,* 1996 vol. 27, pp. 1461-1469, 2001.

[44] A. Lorenz, H.-J. Sommerfeld, M. Garcia-Schurmann, S. Philippou, T. Senge, and H.Ermert, "A new system for the acquisition of ultrasonic multi compression strain Images of the human prostate in vivo,"*Ultrasonics, Ferroelectrics and Frequency. Control,IEEE Transactions on,* vol. 46, pp. 1147-1154, 1999. pp. 286-294.

[45] L. Coutts, J. Bamber, N. Miller, and P. Mortimer, "Ultrasound elastography of the skin and Subcutis under surface extensive loading," *Ultrasound,* vol. 14, pp. 161-166, 2006.

[46] M. W. Gilbertson and B. W. Anthony, "Ergonomic control strategies for a handheld force-Controlled ultrasound probe," in*Intelligent Robots and Systems*

(IROS), 2012 IEEE/RSJ International Conference on, 2012, pp. 1284-1291.

[47] M. Fortin, M. D. Buschmann, M. J. Bertrand, F. S. Foster, and J. Ophir, "Cross-correlation of ultrasound A-lines to obtain dynamic displacement profiles within poroelastic materials undergoing stress relaxation," in *Medical Imaging 2000*,

[48] R. Righetti, J. Ophir, S. Srinivasan, and T. A. Krouskop, "The feasibility of using elastography for imaging the Poisson's ratio in porous media," *Ultrasound in medicine & biology,* vol. 30, pp. 215-228, 2004.

[49] S. P. C. Marques and G. J. Creus, Computational Viscoelasticity, Springer Briefs in Computational Mechanics, Springer 2012.

[50] M. L. Oyen, "Spherical indentation creep following ramp loading," *Journal of Materials Research,* vol. 20, pp. 2094-2100, 2005.

[51] S. R. Aglyamov, S. Park, Y. Ilinskii, and S. Y. Emelianov, "Ultrasound imaging of soft tissue shear viscosity," in *Ultrasonics,2003 IEEE Symposium on*, 2003, pp. 937-940.

[52] G. Montaldo, M. Tanter, J. Bercoff, N. Benech, and M. Fink, "Coherent plane-wave compounding for very high frame rate ultrasonography and transient elastography,"*IEEE Trans. Ultrason. Ferroelectr. Freq.Control,* vol. 56, pp. 489-506, 2009.

[53] R. Erkamp, S. Emelianov, A. Skovoroda, X. Chen, and M. O'Donnell, "Exploiting strain-hardening of tissue to increase contrast in elasticity imaging," *in Ultrasonics Symposium,2000 IEEE, 2000, pp. 1833-1836.*

[54] R. Q. Erkamp, S. Y. Emelianov, A. R. Skovoroda, and M. O'Donnell, "Nonlinear elasticity imaging: theory and phantom study," *Ultrasonics, Ferroelectrics, and Control, Frequency IEEE Transactions on*, vol. 51, pp. 532-539, 2004.

[55] H. Eskandari, S. E. Salcudean, and R. Rohling, "Viscoelastic parameter estimation based on spectral analysis," *Ultrasonics, Ferroelectrics, and Frequency Control, IEEE Transactions on*, vol. 55, pp. 1611-1625, 2008.

[56] H. Ponnekanti, J. Ophir, and I. Cespedes, "Axial stress distributions between coaxial compressors in elastography: an analytical model," *Ultrasound in medicine & biology*, vol. 18, pp. 667-673, 1992.

[57] S. P. Nair, X. Yang, T. Krouskop, and R. Righetti, "Performance analysis of a new real-time elastographic time constant estimator," *Medical Imaging, IEEE Transactions on*, vol. 30, pp. 497-511, 2011.

[58] M. Fortin, M. D. Buschmann, M. J. Bertrand, F. S. Foster, and J. Ophir, "Cross-correlation of ultrasound A-lines to obtain dynamic displacement profiles within poroelastic materials undergoing stress relaxation," in *Medical Imaging 2000*, 2000,

[59] S. Srinivasan, J. Ophir, and S. Alam, "Elastographic imaging using staggered strain estimates," *Ultrasonic imaging*, vol. 24, pp. 229-245, 2002.

[60] A. Race, N. D. Broom, and P. Robertson, "Effect of loading rate and hydration on the mechanical properties of the disc," *Spine*, vol. 25, pp. 662-669, 2000.

[61] F. W. Mauldin Jr, M. Haider, E. G. Loboa, R. H. Behler, L. E. Euliss, T. W. Pfeiler, and C.M. Gallippi, "Monitored steady-stateexcitation and recovery (MSSR) radiation force imaging using viscoelastic models," *Ultrasonics, Ferroelectrics, and Frequency Control, IEEE Transactions on*, vol. 55, pp. *1597-1610, 2008.*

[62] C. Pellot-Barakat, M. Sridhar, K. K. Lindfors, and M. F. Insana, "Ultrasonic elasticity imaging as a tool for breast cancer diagnosis and research," *Current Medical Imaging Reviews*, vol. 2, pp. 157-164, 2006.

[63] M. Z. Kiss, T. Varghese, and T. J. Hall, "Viscoelastic characterization of in vitro canine tissue," *Physics in medicine and biology*, vol. 49, p. 4207, 2004.

[64] H. Murata, N. Taguchi, T. Hamada, and J. F. McCabe, "Dynamic viscoelastic properties and the age changes of long-term soft denture liners," *Biomaterials*, vol. 21, pp. 1421-1427, 2000.

[65] M. Ueshige, Y. Abe, Y. Sato, K. Tsuga, Y. Akagawa, and M. Ishii, "Dynamic viscoelastic properties of antimicrobial tissue conditioners containing silver–zeolite," *Journal of dentistry*, vol. 27, pp. 517-522, 1999.

[66] J. Gladden, A. Gamble, C. Skelton, and J. Mobley, "Shear waves in viscoelastic wormlike micellar fluids over a broad concentration range," *The Journal of the Acoustical Society of America*, vol. 131, pp. 2063-2067, 2012.

[67] M. F. Insana, J. Liu, M. Sridhar, and C. Pellot-Barakat, "Ultrasonic mechanical relaxation imaging and the material science of breast cancer," in *Ultrasonics Symposium, 2005 IEEE*, 2005, pp. 739-742.

[68] Fung Y 1993 Biomechanics: Mechanical Properties of Living Tissues (Berlin:Springer)

[69] C. Amador, A. Nabavizadeh, R. Kinnick, and M. Fatemi, "Loading ramp effects in 2014, uniaxial compression creep device," in *Ultrasonics Symposium (IUS),*

2014 IEEE International, pp. 2320-2322.

[70] H. Eskandari, S. E. Salcudean, R. Rohling, and J. Ohayon, "Viscoelastic characterization of soft tissue from dynamic finite element models, " *Physics in medicine and biology*, vol.53, p. 6569, 2008.

[71] *Breast Cancer Facts & Figures 2015-2016. - American Cancer Society*.

[72] *Ganong's Review of Medical Physiology (24 ed.). p. 619. ISBN 0071780033.*

[73] S. Raza, A. L. Goldkamp, S. A. Chikarmane, and R. L. Birdwell, "US of Breast Masses Categorized as BI-RADS 3, 4, and 5: Pictorial Review of Factors Influencing Clinical Management 1," *Radiographics*, vol. 30, pp. 1199-1213,2010

[74] Du H, Liu J, Barakat C, Insana MF. Optimizing multicompression approaches to breast elasticity imaging. *IEEE Trans UltrasonFerroelec Freq Control 2006;53:90–99.*

Appendix:

Benign:

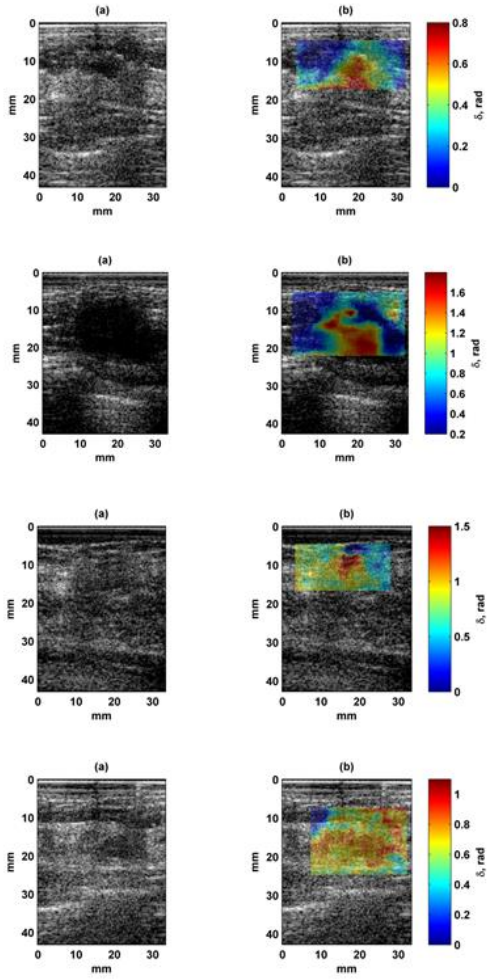

Malignant: